https://doi.org/10.5194/egusphere-2025-5923
Preprint. Discussion started: 23 December 2025

Capability of current observing systems to monitor CH_4 emissions from the regional to the global scales

Nicole Montenegro[1,*], Antoine Berchet[1], Adrien Martinez[1], Joël Thanwerdas[2], Philippe Bousquet[1], Isabelle Pison[1], and Marielle Saunois[1]

[1]Laboratoire des Sciences du Climat et de l'Environnement, LSCE/IPSL, CEA-CNRS-UVSQ, Université Paris-Saclay, F-91191 Gif-sur-Yvette, France
[2]Empa, Swiss Federal Laboratories for Materials Science and Technology, Dübendorf, Switzerland
[*]Correspondance: nicole.montenegro@lsce.ipsl.fr

Abstract. Top-down methane (CH_4) flux estimates involve large uncertainties stemming from three main sources: (1) the coverage of the observing system, (2) systematic and random errors in the observation data and the priors and (3) errors in the atmospheric transport model. Quantifying these uncertainties is challenging, and methodological studies suggest they can be substantial. While global-scale uncertainties in total CH_4 emissions are relatively small ($\pm 5\%$), they increase significantly at regional scales exceeding $\pm 20\%$ for high latitudes. Differences in satellite and in situ measurement uncertainties, as well as variations in data density, further influence the precision of CH_4 flux estimates. Sectoral disaggregation of uncertainties improves error attribution, leading to more reliable regional flux assessments and trend detection. Its benefits are amplified in high-emission regions due to larger absolute uncertainties and more complex source mixtures. In this work, we use Observing System Simulation Experiments (OSSEs) to determine the capability of current observing systems to retrieve surface fluxes of CH_4 and to quantify the magnitude of their associated uncertainties. The experiments are conducted within the Community Inversion Framework (CIF) over the period from June 2018 to June 2020, with the atmospheric transport model LMDZ-SACS, applying a Bayesian approach that optimally combines CH_4 observations, fluxes, covariance matrices, and input parameters. CH_4 fluxes are perturbed using a Monte Carlo method, generating a 10-member ensemble. OSSEs area conducted over 18 regions in two cases using: (1) total flux and (2) eleven sectorial fluxes. Assimilated observations include GOSAT-1-NIES, GOSAT-1-Leicester, IASI-MetOp-A, TROPOMI-WFMD and in situ measurements, together with their combinations. OSSE results are analyzed at both the regional and sectorial scales. The results show that methane estimates based-in situ observations achieve the strongest performance, particularly in the Northern Hemisphere, reducing uncertainties of more than 30% in regions such as the USA, Canada, Europe, the Middle East, China, and Korea–Japan. Complementarity between observation systems is essential: the combination of in situ data with GOSAT-NIES consistently outperforms TROPOMI-WFMD, achieving over 30% uncertainty reduction in South Asia, a region of high CH_4 emissions. Finally, sectoral based inversions demonstrate that optimizing individual sectors, especially agriculture and oil and gas, yields larger reductions in uncertainty than total flux optimization alone. These findings highlight the value of combining observation systems and sectoral approaches for improving methane flux estimates at the global and regional scales.

https://doi.org/10.5194/egusphere-2025-5923
Preprint. Discussion started: 23 December 2025

1 Introduction

Global methane (CH_4) mixing ratio have risen since the pre-industrial era from around 800 ± 50 ppb to 1933.5 ppb in May 2025 (Etheridge et al., 1988; Lan et al., 2022). This sharp increase, more than doubling the pre-industrial era levels, highlights the impact of anthropogenic sources on atmospheric methane levels. CH_4 is the second-largest anthropogenic contributor to climate radiative forcing after carbon dioxide (CO_2), CH_4 emissions accounting for approximately 31% of the total effective radiative forcing from greenhouse gases and their precursors (3.84 Wm^{-2} [3.46 to 4.22]) over the industrial era (1750–2019) (Forster et al., 2021; Szopa et al., 2021a). These estimates include both direct and indirect effects, such as ozone formation, increased stratospheric water vapor, impacts on aerosols, as well as on the lifetimes of HCFCs and HFCs (Myhre et al., 2014; O'Connor et al., 2021). Methane has a total atmospheric lifetime of approximately 9.1 ± 0.9 years (Szopa et al., 2021b). A one-year pulse of present-day greenhouse gas emissions leads to a global temperature increase of 0.028°C over the following 10 years due to methane, making it the largest temperature response among all greenhouse gases (Szopa et al., 2021b). These characteristics make methane reduction a promising short-term mitigation strategy, highlighting the need for more accurate global estimates of methane sources and sinks.

Methane fluxes can be estimated using two complementary approaches: the bottom-up method, based on inventories and direct estimations from models, and the top-down method, which infers sources and sinks from atmospheric methane observations.

In the top-down approach, various sources of uncertainty must be considered, including systematic and random uncertainties in the d systematic errors in the model and smoothing errors associated with uncertainty in prior emissions and spatial resolution (Worden et al., 2022).

At the global scale, uncertainties in this approach have been estimated to be below $\pm 5\%$ for a given OH field, but they increase regionally: $\pm 7\%$ in the tropics, $\pm 12\%$ in mid-latitudes, and $> \pm 20\%$ in high latitudes (Saunois et al., 2025). In terms of sectoral emission uncertainties, decadal budget estimates from bottom-up inventories suggest ranges of 20–35% for agriculture, waste, and fossil fuels; 50% for biomass burning and natural wetland emissions; and up to 100% for other natural sources (Saunois et al., 2025). These priors are used in top-down inversions, meaning that these uncertainties propagate into the resulting CH_4 flux estimates (Saunois et al., 2025).

Methane mixing ratio are measured locally at the surface using discrete air samples regularly collected or continuous measurements from national and international networks such as the United States National Ocean and Atmospheric Administration Global Monitoring Laboratory (NOAA; Dlugokencky et al., 2020), Integrated Carbon Observation System (ICOS; Lund Myhre et al., 2022), Commonwealth Scientific and Industrial Research Organisation (CSIRO; Francey et al., 1996), Advanced Global Atmospheric Gases Experiment (AGAGE; Prinn et al., 2018), University of California, Irvine (UCI; Simpson et al., 2012), and the Global Environmental Database of National Institute for Environmental Studies (NIES), Japan (Global Environmental Database (GED), 2024). Instruments measuring CH_4 provide reliable measurements, with a precision of approximately 1.5 ppb and an experimental uncertainty of around 3 ppb (Masarie et al., 2001; Andrews et al., 2014). Despite high emissions in the tropics, surface stations are sparse, with 80% located in the Northern Hemisphere.

https://doi.org/10.5194/egusphere-2025-5923
Preprint. Discussion started: 23 December 2025

Satellite platforms provide measurements of the column-averaged dry air mole fraction of methane (XCH_4) in cloud-free conditions, offering broader global coverage than surface networks. Thermal infrared (TIR) satellite observations are sensitive to CH_4 mixing ratios in the middle to upper troposphere due to the thermal contrast between the atmosphere and the surface, whereas shortwave infrared (SWIR) observations are more sensitive to near-surface CH_4, where emissions originate.

SWIR observations are limited at high latitudes in winter due to weak solar radiation, and both SWIR and TIR measurements are sensitive to clouds (Zhang et al., 2018; Palmer et al., 2021; Jacob et al., 2016). Satellite instruments classified as area flux mappers are characterized as high precision instruments (< 1% precision) with a pixel size of 0.1-10 km and designed to quantify total methane emissions at the regional to the global scales (Jacob et al., 2022). Within this group, in the SWIR spectrum, three main missions stand out: the SCIAMACHY instrument on ESA's ENVISAT satellite (2002–2012) (Gottwald et al., 2011); the Japan's GOSAT mission, dedicated to measuring greenhouse gases (GOSAT-1 launched in 2009, followed by GOSAT-2 in 2018), equipped with TANSO-FTS and TANSO-CAI (Yokota et al., 2009; Yoshida et al., 2023); and the TROPOMI instrument aboard the Copernicus Sentinel-5 Precursor (S5P), launched in 2017, which provides higher spatial resolution and daily global coverage compared to previous satellite missions (Veefkind et al., 2012).

In the TIR spectrum, the following satellites stand out in the retrieval of XCH_4 : The Tropospheric Emission Spectrometer (TES) and Infrared Atmospheric Sounding Interferometer (IASI). TES was launched aboard the Earth Observing System's Aura satellite in 2004 and completed its mission in 2018 (Beer et al., 2001). TES exhibited a high sensitivity to CH_4 variations in the free atmosphere, making its data valuable for constraining the role of tropical wildfires (Worden et al., 2013). The first, IASI-MetOp-A, operated from 2006 to 2021, while the current IASI-MetOp-B and IASI-MetOp-C have been in orbit since 2012 and 2018, respectively. IASI provides methane profile data in both the upper and lower troposphere (Clerbaux et al., 2007).

Satellite data, such as from GOSAT and TROPOMI, offer an extensive spatial coverage, particularly over regions with sparse surface observations like the tropics. This broader coverage helps better constrain methane flux estimates (Saunois et al., 2025).

The comparison between satellite-based and surface-based inversions reveals significant differences in methane flux estimates, with regional variations depending on data sources and geographic location (Saunois et al., 2025). For instance, in Saunois et al. (2025), methane emissions estimated by satellite-based inversions are higher than those derived from surface-based inversions over the tropical zone by approximately 15–30 Tg CH_4 $year^{-1}$, whereas in the northern mid-latitudes, the estimates from inversions-based on-situ surface data are larger by 2–36 Tg CH_4. Similarly, using GOSAT data, Tsuruta et al. (2025) estimated that the retrieved fluxes in the Southern Hemisphere were about 15–30 Tg CH_4 $year^{-1}$ higher than the corresponding fluxes derived from surface measurements. However, despite these regional discrepancies, some studies have shown overall consistency between satellite- and surface-based inversion estimates when examined at broader spatial and temporal scales. For example, Palmer et al. (2021), found that long-term methane emission estimates inferred from GOSAT data (2010–2019) are largely consistent with those derived from surface-based observations on continental scales, although discrepancies emerge at the sub-continental scales due to differences in data density and biases. TROPOMI, on the other hand, offers denser observational coverage but can exhibit regional biases — for example, over southeast China, where complex surface conditions and frequent cloud cover can lead to uncertainties or misattribution in the inferred methane fluxes (Qu et al., 2021).

https://doi.org/10.5194/egusphere-2025-5923
Preprint. Discussion started: 23 December 2025

The combination of surface and satellite data often results in stronger adjustments to the vertical distribution of atmospheric methane, especially in the tropics and high latitudes, to varying extents depending on the region (Monteil et al., 2013).

Recent studies have shown that using both GOSAT and surface data can significantly improve the accuracy of methane emission estimates, particularly in regions such as East Asia, where the two datasets provide complementary information (Liang et al., 2023). However, discrepancies remain with TROPOMI-based inversions showing higher emissions in some areas, while GOSAT-based inversions tend to be more consistent with surface and TCCON data in regions like northern India and eastern China (Qu et al., 2021).

These differences highlight the need to better understand how observational coverage and inversion configurations influence emission estimates and their associated uncertainties.

In variational atmospheric inversion frameworks, quantifying the uncertainty of posterior emission estimates remains a substantial challenge. This task is computationally intensive because it requires characterizing how observational and model errors propagate through the inversion system, a process that often demands far more resources than estimating the emissions themselves, making it practically infeasible with a 4D-Var approach. In this context, the Observing System Simulation Experiment (OSSE) emerges as a highly valuable approach for estimating posterior emission uncertainties (Hungershoefer et al., 2010).

The aim of the present study is to determine the capability of current observing systems to retrieve surface fluxes of CH_4 at the regional and sectoral scales using OSSEs. Specifically, OSSEs are conducted within the Community Inversion Framework (CIF, Berchet et al. (2021)) over the period June 1, 2018 to June 30, 2020, using a 4D-Var approach, to assess the capability of each observing system to retrieve true fluxes and to reduce uncertainties on fluxes. Two cases are performed 1) one where total net flux is optimized at the pixel resolution and 2) one where 11 sectoral flux categories are optimized at the pixel resolution. The experiments are based on the atmospheric transport model LMDZ with a 2.5° x 1.27° grid resolution (Hourdin et al., 2020). In the experiments, CH_4 fluxes are perturbed using a random distribution based on the Monte Carlo method, applied either to the total net flux or to each sectoral flux.

Section 2 introduces the dataset of in situ and satellite observations, Section 3 describes the atmospheric inversion experiments conducted in the CIF using the LMDZ model within the OSSE framework. Section 4 presents the results, focusing on the observational potential of individual systems to improve methane flux estimates and to reduce the uncertainty of recovered fluxes, as well as on their complementarity, with a regional perspective that considers both total flux experiments and sectoral disaggregation. Finally, Section 5 outlines the limitations of the experiments, highlights missing components, and discusses the contribution of this research to global methane budget assessments.

2 Input data

This section presents the datasets used as inputs to the atmospheric inversion framework, including satellite retrievals of column-averaged atmospheric (XCH_4), in situ surface CH_4 mixing ratios, prior methane fluxes and prescribed fields and initial conditions.

https://doi.org/10.5194/egusphere-2025-5923
Preprint. Discussion started: 23 December 2025

2.1 Satellite observations

The satellite instruments considered in this study are GOSAT-TANSO, MetOp-A IASI and the Sentinel-5P TROPOMI. These platforms provide complementary information on atmospheric methane, with differences in spectral range, sensitivity, spatial coverage, and temporal resolution. It is important to keep in mind that, within our OSSE framework, we do not assimilate real retrievals from these instruments. Instead, we generate synthetic observations (pseudo-data) that mimic the spatio-temporal sampling and structural characteristics of the retrievals. Further details on the synthetic data are provided in Section 3.6.

2.1.1 CH_4 platforms and instruments

GOSAT-TANSO

The GOSAT mission, led by the Japanese Space Agency (JAXA) in collaboration with the NIES, GOSAT carries the TANSO-FTS instrument, which offers a high spectral resolution and wide spectral coverage from visible light to thermal infrared. It was launched in January 2009 into a sun-synchronous orbit at an altitude of 666 km, with a ground pixel diameter of 10.5 km and a revisit of 3 days at a local time of 13:00. Methane columns are retrieved from the SWIR band 5900-6150 cm^{-1} (Yokota et al., 2009).

METOP-A IASI

IASI, launched by EUMETSAT in October 2006 on board MetOp-A, operates in a polar orbit with a period of about 10 minutes, providing near-global coverage twice per day. Over latitudes around 60°, overpasses occur at approximately 9:00–10:00 and 21:00–22:00 local solar time, with a repeat cycle of 29 days and a spatial resolution of 12 km (Clerbaux et al., 2009). Methane retrievals from the IR ν_4 band (~7.7 μm, 1306 cm^{-1}) are mainly sensitive to mid-tropospheric CH_4 (Crevoisier et al., 2009). In synchronization with IASI, the AMSU (Advanced Microwave Sounding Unit) instrument provides complementary microwave observations, which are particularly sensitive to temperature (Clerbaux et al., 2009).

In this study, we use only MetOp-A observations. Although IASI instruments also fly on MetOp-B and MetOp-C, including multiple platforms would not provide additional information for our synthetic-data framework. Because the retrievals are simulated, using a single satellite is sufficient to represent the measurement characteristics needed for our experiments.

Sentinel-5P TROPOMI

TROPOMI was lanched in 2017 onboard the Sentinel 5 Precursor (S5P) polar-orbiting satellite. It provides CH_4 colums from the SWIR at the high spatial resolution of 5.5 × 7 km^2 with global daily coverage, crossing at 13:30 mean local solar time. The mission was conducted cooperatively by the European Space Agency (ESA) and the Netherlands as part of the EU Copernicus program (Hu et al., 2016).

https://doi.org/10.5194/egusphere-2025-5923
Preprint. Discussion started: 23 December 2025

2.1.2 Retrievals algorithms

This section presents the retrieval algorithms used in this study.Information on averaging kernels and applications is given in Sect. 3.3.2.

GOSAT-TANSO

The **GOSAT-NIES** data recovered by the NIES, correspond to column-averaged dry-air mole fractions of CH_4 (XCH_4) derived from SWIR radiance spectral data. The SWIR L2 CH_4 retrieval algorithm developed at NIES is a fully physics-based algorithm that explicitly takes into account particle scattering processes in the atmosphere in the calculation of radiative transfer (Yoshida et al., 2013). Less than 10% of the total data collected passes quality control (Someya et al., 2023). The site-to-site bias of GOSAT-NIES data against ground-based TCCON is less than 5 ppb and a single-sounding precision of 10 ppb (Someya et al., 2023; Yoshida et al., 2023). The data used are GOSAT-NIES SWIR V02.96 level 2 (NIES GOSAT Data Archive Service, 2023).

The **GOSAT-Leicester** product from the University of Leicester (England), contains column-averaged dry-air mole fraction of methane (XCH_4) generated from GOSAT Level 1B data version 210.210 using the University of Leicester Full-Physics retrieval scheme (UoL-FP) and the proxy retrieval approach (Parker et al., 2020). The proxy approach is based on the principle that CO_2 and CH_4 have a common absorption band around 1.6 μm and so most atmospheric light scattering and instrumental effects will be similar for both. The proxy method recovers 23.5% of the total data, providing relatively higher coverage than the full physics method, particularly in the tropics and in regions affected by clouds, where the physical method applies stricter filtering (Parker et al., 2020). The overall bias of the Proxy XCH_4 data relative to ground-based TCCON observations is estimated at 9.06 ppb, which is removed from the GOSAT data, therefore assuming unbiased data. The single-sounding precision is 13.72 ppb, with a correlation coefficient of 0.92 relative to TCCON (Parker et al., 2020). The version of GOSAT Proxy XCH_4 used in this study is v9.0 (Parker and Boesch, 2020).

In this study, we selected the NIES and Leicester University retrievals, as they provide complementary perspectives on the potential of each retrieval. GOSAT-NIES offers a high-precision physical approach, while GOSAT-Leicester provides a proxy-based product with broader coverage.

METOP-A IASI

In this study, we use the XCH_4 total column retrieval product from the Non-Linear Inversion Scheme (NLIS v9.1) developed by the Laboratoire de Météorologie Dynamique (LMD),where IASI and AMSU channels are combined to decorrelate their respective signals through a non-linear inference scheme based on a neural network, with a precision estimated at about 16 ppbv (∼0.9%) (Crevoisier et al., 2009). XCH_4, as well as the averaging kernel, among other variables, are provided by the AERIS Atmospheric composition data products (AERIS Atmospheric Data Centre, 2021).

https://doi.org/10.5194/egusphere-2025-5923
Preprint. Discussion started: 23 December 2025

In our OSSE framework, we select the IASI-LMD product for methane observations, rather than the IASI-RAL retrieval (Siddans et al., 2017). The primary reason is that IASI-LMD provides mid-tropospheric XCH_4 columns with well-characterized averaging kernels and associated observation errors, which are directly compatible with the forward model and synthetic observation generation in our OSSE (Crevoisier et al., 2009). While IASI-RAL (Siddans et al., 2017) aims to retrieve the full column, including the lower troposphere, the sensitivity close to the surface is inherently limited in the thermal infrared (TIR) and the retrieval in this layer is more strongly influenced by regularization and assumptions, resulting in larger uncertainties.

Sentinel-5P TROPOMI

In this study, the TROPOMI-WFMD product version 1.8 developed by the University of Bremen is used. It is obtained using the scientific retrieval algorithm Weighting Function Modified Differential Optical Absorption Spectroscopy (WFM-DOAS) and undergoes a strict machine learning (ML) classifier filter, which allows for the reduction of large systematic errors (Schneising et al., 2019). A site-to-site comparison between TCCON and TROPOMI-WFMD v1.8 yielded a bias of 5.2 ppb and a precision of 12.4 ppb (Schneising et al., 2019). Data are obtained from Schneising et al. (2023)

Among the available TROPOMI retrievals – SRON (Lorente et al., 2021), WFMD (Schneising et al., 2023), and the BLENDED product (Balasus et al., 2023) – we selected WFMD because it provides the largest coverage, with approximately 30% more observations compared to SRON or BLENDED, thereby offering an upper-limit scenario for the observational potential of TROPOMI. WFMD exhibits larger observational errors than the other products, which allows us to test inversion performance under more challenging error conditions. This combination of maximum coverage and maximum noise defines an "extreme" case, suitable for exploring the sensitivity of the OSSE to both observational density and error characteristics. It is important to note that in the context of an OSSE, systematic differences between retrievals (e.g., biases related to aerosol scattering or surface albedo sensitivity) are not explicitly represented, since pseudo-observations are generated directly from the modeled atmosphere using averaging kernels and prescribed error statistics.

A comprehensive comparison of the three TROPOMI products has already been carried out in Sicsik-Paré et al. (2025) using regional inversions over Europe and evaluating the performance of SRON (v2.4), BLENDED (v1.0), and WFMD (v1.8) products.

2.1.3 Super-observations

Satellite XCH_4 are aggregated according to the horizontal resolution of the LMDZ model of 144x142 pixels (2.5° in longitude and 1.27° in latitude) and its physical parameterization time step of 20 minutes. From this aggregation, we selected the median XCH_4 and its associated instrumental error. Figure A1, in Appendix, illustrates the spatial distribution of the average instrumental error of these super-observations for 2019. The aim of building super-observations is to reduce the amount of data to be assimilated while retaining a relevant amount of information and, potentially, avoiding the assimilation of incompatible or redundant information within a pixel at a given time-step. This approach also helps satisfy the common assumption of uncorrelated observation errors, which becomes difficult when many observations are available within a narrow time window.

https://doi.org/10.5194/egusphere-2025-5923
Preprint. Discussion started: 23 December 2025

For the year of our experiment analysis (2019), we have a global dataset of 73,276 superobservations for GOSAT-NIES, 214,769 observations for GOSAT-Leicester, 1,208,184 observations for IASI-Metop-A and 1,129,139 observations for TROPOMI-WFMD whose global spatial distributions are presented in Figure 1. Breakdown of super-observation counts by region and observing system is provided in the Appendix (Figure A3).

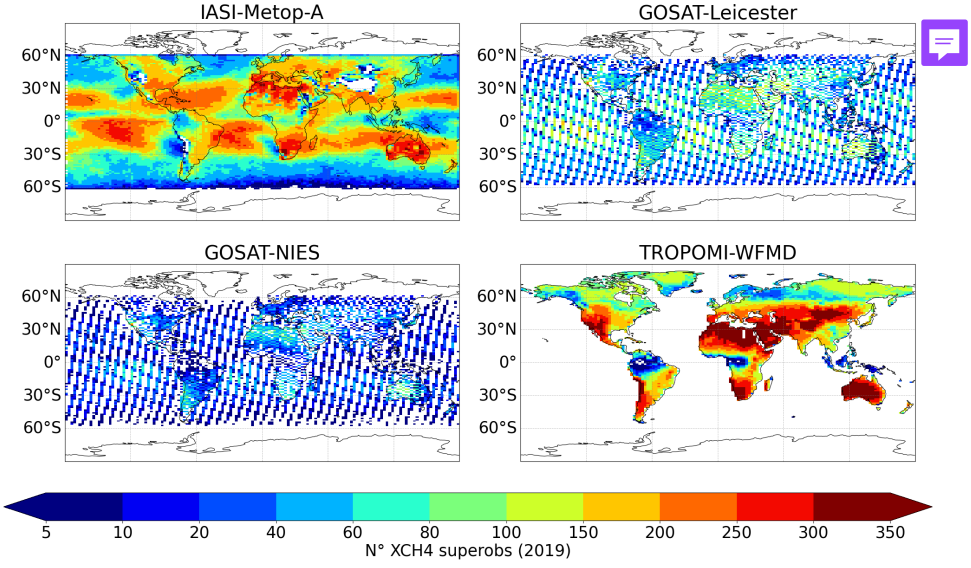

Figure 1. Number of superobservations by pixel for the year 2019 from each XCH4 retrieval product: IASI-Metop-A, GOSAT-Leicester, GOSAT-NIES and TROPOMI-WFMD.

2.2 Surface CH_4 mixing ratio

In this study, we use in situ observations from 155 stations: NOAA (110), ICOS (36), and CSIRO (9).

- **NOAA network**: we use observations obtained from ObsPack-CH4 GLOBALVIEWplus version 4.0 (2021-10-14) (Schuldt et al., 2021a) and ObsPack-CH4 NRTv3.0 version 2021-05-18 (Schuldt et al., 2021b).
- **ICOS**: we take Near Real-Time (Level 1) Atmospheric Greenhouse Gas Mole Fractions of CO_2, CO, and CH_4, with growing time series starting from the latest Level 2 release (ICOS Research Infrastructure, 2018).
- **CSIRO**: we recovered data from the World Data Centre for Greenhouse Gases (WDCGG) of the WMO Global Atmospheric Watch program (WMO-GAW Programme, 2023).

2.2.1 Filtering of surface data

In situ observations are processed through a data filtering procedure based on the principles of Ritter (2023). Outliers were identified and removed using a seasonal–trend decomposition with residual analysis. More precisely, observations exceeding three times the residual standard deviation were flagged as outliers and excluded.

https://doi.org/10.5194/egusphere-2025-5923
Preprint. Discussion started: 23 December 2025

For mountain stations (above 800 m), observations are averaged between 00:00 and 06:00 local time, when the nocturnal stable layer ensures that measurements are representative of background mixing ratios (Lopez et al., 2015). For non-mountain sites, data are averaged in the afternoon (12:00–18:00 local time), when the boundary layer is typically well mixed and measurements best reflect regional background conditions (Stull, 1988).

Figure 2 illustrates surface stations measuring CH_4 in 2019 after filtering and averaging. The global methane observation network is largely concentrated in the Northern Hemisphere, particularly across the United States and Europe. In fact, 83 % of the stations are located north of the equator, with a median mixing ratio of 1.96 ppm. Consequently, the Southern Hemisphere accounts for only 8 % of the total number of observations, with a lower median mixing ratio of 1.82 ppm. The mean observational error of the data used is 3.11 ppb. More details about the stations used are available in Appendix Table A1 and A2.

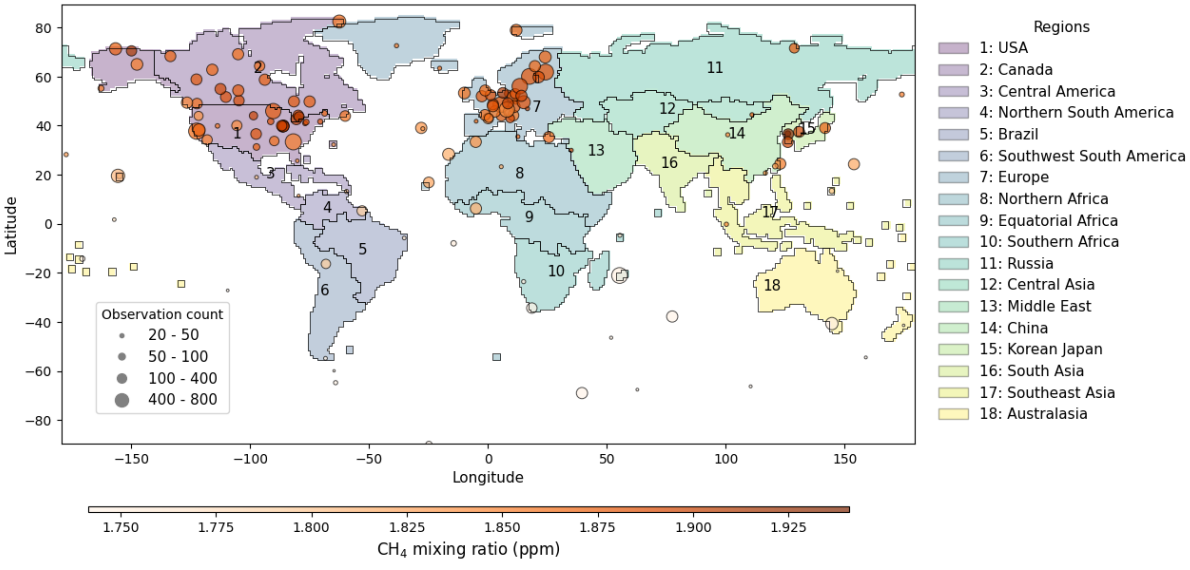

Figure 2. Map of the 18 continental regions used in this study, based on Saunois et al. (2025). Surface stations measuring methane are shown as red dots, with marker size representing the number of observations in 2019 after filtering and averaging (see Section 2.2.1) and color indicating the mean atmospheric mixing ratio for that year.

2.3 Prior fluxes

We consider eleven sectoral fluxes, of which six are anthropogenic (agriculture, biofuels, biomass burning, coal, oil-gas-industry and waste) and five are natural (geological, soils, ocean, termites, wetlands), as shown in Appendix Figure A4.

Anthropogenic methane emissions are derived from the Emissions Database for Global Atmospheric Research (EDGAR), compiled by the European Commission Joint Research Centre (EC-JRC) and the Netherlands Environmental Assessment Agency (PBL). The datasets used are EDGAR v6.0 (Monforti Ferrario et al., 2021) and EDGAR v7.0 (Crippa et al., 2021).

https://doi.org/10.5194/egusphere-2025-5923
Preprint. Discussion started: 23 December 2025

Since EDGAR v7.0 provides only annual gridded fluxes, monthly fluxes are generated using the temporal variability of EDGAR v6.0.

The original EDGAR fluxes have a native horizontal resolution of $0.1° \times 0.1°$ at the global scale. For this study, an area-weighted interpolation is applied to aggregate them to $1° \times 1°$, ensuring mass conservation.

The sectors considered in this study correspond to an aggregation of EDGAR categories:

- Agriculture: enteric fermentation, manure management and rice.
- Biofuels: energy for buildings.
- Emissions from biomass burning are derived from Global Fire Assimilation System (GFAS) data (Kaiser et al., 2012). Agricultural waste burning is included in this category and it has been excluded from EDGARv6 to avoid double counting.
- Coal: coal production.
- Oil, gas and industry: gas and oil, non-road transport, road transport, chemical processes, combustion from manufacturing, iron and steel production, power industry, oil refineries and transformation industry and fossil fuel fires.
- Waste: solid waste landfill, solid waste incineration and wastewater treatment.

The emissions from natural sources considered in this study were as follows:

- Climatological emissions from wetlands, termites, ocean and geological are obtained from Saunois et al. (2025).
- Coastal and oceanic sources are taken from Weber et al. (2019).
- For the soil uptake, we use the estimates calculated by the VISIT model (the Vegetation Integrative SImulator for Trace gases) (Ito and Inatomi, 2012), which is an integrated model for simulating biogeochemical interactions based on radiation, water, carbon, and nitrogen schemes.

Figure 3 presents the total and sectoral CH_4 emissions for the 18 regions previously defined in Figure 2. China is the largest contributor to global methane emissions in 2019, followed by Russia and Southeast Asia, aligned with Saunois et al. (2025). The largest emitting regions are characterized by different dominant sectors: in Southeast Asia, agriculture accounts for 60% of emissions; in China, coal contributes 32%; and in the Middle East, the oil, gas, and industrial sector represents 63% of emissions.

https://doi.org/10.5194/egusphere-2025-5923
Preprint. Discussion started: 23 December 2025

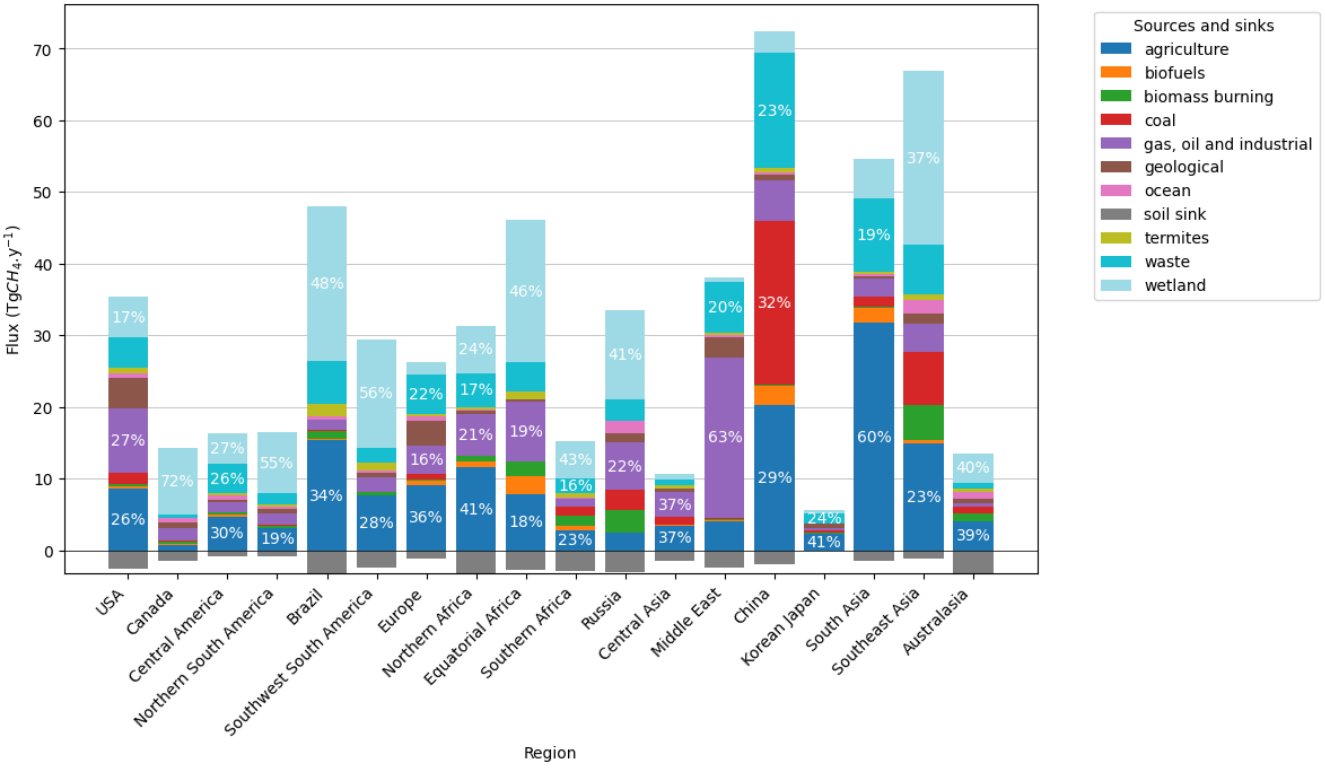

Figure 3. Methane emissions from 10 sectors and soil uptake for 2019, for the 18 regions defined in [illegible]elative to the total regional fluxes for that year. Percentages indicate each sector's contribution to the corresponding regional total emissions.

2.4 Prescribed fields and initial conditions

Our study relies on atmospheric simulations that require both prescribed fields and initial conditions. These components are detailed below.

Meteorology: meteorological fields (e.g. mass fluxes and temperature) are pre-computed by the online version of LMDZ. In this setup, horizontal winds are nudged towards ERA5 analyses and subsequently used to drive the offline model, which substantially reduces the computational burden of transport calculations.This configuration greatly reduces the computational cost of transport simulations relative to the fully coupled (online) version, because the dynamical fields (e.g., winds, temperature, and mass fluxes) are precomputed and prescribed rather than computed interactively at each time step.

Prescribed chemistry: mixing ratios of oxidants involved in CH_4 chemistry (OH, $O(^1D)$, and Cl) are prescribed from LMDZ-INCA (INteraction between Chemistry and Aerosol) simulations (Hauglustaine et al., 2004). These tracers are not transported or updated through chemical production/loss, but are only used to compute reaction rates at each model time step (Thanwerdas et al., 2022).

https://doi.org/10.5194/egusphere-2025-5923
Preprint. Discussion started: 23 December 2025

Initial conditions: 3D fields of CH_4 dry-air mole fraction were initialized in July 2018 from a spin-up inversion with LMDZ-SACS, following the methodology of Locatelli et al. (2015). The inversion assimilated about 120 global background stations from 1999 to 2018, ensuring observation-constrained initial conditions for the simulations.

3 Methods

This section outlines the atmospheric inversion framework employed, including the Bayesian four-dimensional variational (4D-Var) and LMDz-SACS model setup. It also describes the method used to derive satellite-equivalent XCH_4 from satellite data. In addition, the design of the prior ($\mathbf{B}$) and observational ($\mathbf{R}$) error covariance matrices is presented, along with the estimation of observation sensitivities to surface emissions and the configuration of Observing System Simulation Experiments (OSSEs). Sensitivity experiments and OSSEs are performed using the Community Inversion Framework (CIF).

The CIF is a collaborative platform initiated by members of the atmospheric greenhouse gas inversion community. It aims at providing a unified environment for performing inverse modeling studies by integrating the control variables, the chemistry–transport model and its input parameters, observational datasets, error covariance matrices ($\mathbf{B}$ and $\mathbf{R}$), and the chosen minimization algorithm.

Finally, the methodology used to estimate uncertainties and to quantify the ability of the observing systems to recover target emissions is also presented.

3.1 Bayesian inversion framework and model description

3.2 General framework

Our study assesses the potential of satellite and in situ data in atmospheric inversions to retrieve CH_4 fluxes at the regional and global scales. The inversion method used is a 4D-Var approach, which seeks the minimum of the cost function $J(\mathbf{x})$, equivalently the maximum a posteriori estimate of the state under the assumption of Gaussian prior and observation errors. In this framework, the posterior distribution is $p^{\mathrm{a}}(\mathbf{x}) \sim \mathcal{N}(\mathbf{x}^{\mathrm{a}}, \mathbf{A})$, where $\mathbf{x}^{\mathrm{a}}$ is the analysis state and $\mathbf{A}$ is the posterior error covariance matrix (Berchet et al., 2021).

$$J(\mathbf{x}) = \frac{1}{2}(\mathbf{x}-\mathbf{x}^{\mathrm{b}})^T\mathbf{B}^{-1}(\mathbf{x}-\mathbf{x}^{\mathrm{b}}) + \frac{1}{2}(\mathbf{y}^{\mathrm{o}}-\mathcal{H}(\mathbf{x}))^T\mathbf{R}^{-1}(\mathbf{y}^{\mathrm{o}}-\mathcal{H}(\mathbf{x})) \quad (1)$$

With:

- $\mathbf{x}$: the control vector, gathering the variables optimized by the inversion system, including surface monthly CH_4 fluxes (total or sectoral, depending on the experiment) and the initial conditions for CH_4 (3D mixing ratio fields);
- $\mathbf{x}^{\mathrm{b}}$: the *a priori* estimate of $\mathbf{x}$;
- $\mathbf{y}^{\mathrm{o}}$: the vector of observations, including in situ and satellite data;
- $\mathbf{x}^{\mathrm{a}}$: the posterior state vector;

https://doi.org/10.5194/egusphere-2025-5923
Preprint. Discussion started: 23 December 2025

- $\mathcal{H}$: the observation operator linking control variables to the observed ones;
- $\mathbf{B}$: the covariance matrix of prior errors (see section 3.4);
- $\mathbf{R}$: the covariance matrix of observation errors (see section 3.4).

$$J(\mathbf{x}) = \frac{1}{2}(\mathbf{x}-\mathbf{x}^{\mathrm{b}})^T\mathbf{B}^{-1}(\mathbf{x}-\mathbf{x}^{\mathrm{b}}) + \frac{1}{2}(\mathbf{y}^{\mathrm{o}}-\mathcal{H}(\mathbf{x}))^T\mathbf{R}^{-1}(\mathbf{y}^{\mathrm{o}}-\mathcal{H}(\mathbf{x})) \quad (2)$$

The minimum of the cost function $\mathbf{J}(\mathbf{x})$ can be obtained iteratively using a gradient-based descent algorithm, which stops when a predefined convergence criterion is satisfied. The gradient of $\mathbf{J}(\mathbf{x})$ with respect to the control vector $\mathbf{x}$ is expressed as:

$$\nabla J(\mathbf{x}) = \mathbf{B}^{-1}(\mathbf{x}-\mathbf{x}^{\mathrm{b}}) + \mathcal{H}^*\left(\mathbf{R}^{-1}\left(\mathcal{H}(\mathbf{x})-\mathbf{y}^{\mathrm{o}}\right)\right) \quad (3)$$

where $\mathcal{H}^*$ denotes the adjoint operator of $\mathcal{H}$.

3.3 Observation operator and averaging kernels

3.3.1 Chemistry–transport model LMDZ-SACS

The LMDZ model is the atmospheric component of the IPSL-CM6A-LR coupled model developed at the Laboratoire de Météorologie Dynamique (LMD) (Hourdin et al., 2020). In this study, we use its offline configuration, coupled with the Simplified Atmospheric Chemistry System (SACS; Pison et al. 2009), which represents the methane oxidation chain. The model runs at a horizontal resolution of 144 × 142 grid points (2.5° longitude × 1.27° latitude), with 79 hybrid sigma-pressure vertical levels and dynamic and physical time steps of 10 and 20 minutes, respectively (Hourdin et al., 2020). LMDZ includes the Emanuel (Emanuel, 1991) deep convection scheme, coupled with a representation of cold pools generated by the evaporation of precipitation (Grandpeix and Lafore, 2010; Grandpeix et al., 2010). The thermal plume model can also be activated in regions of strong inversion (Hourdin et al., 2019), which is particularly relevant for boundary-layer mixing. Our simulations require prescribed fields and initial conditions, described in Sect. 2.4.

The observation operator links the model state to the different types of observations used in this study. For in-situ measurements, H samples the simulated 4D fields at the exact location (latitude and longitude) and time of each station and extracts the modelled methane mixing ratio at the appropriate model level after filtering and temporal averaging (Sect. 2.2.1). For satellite retrievals, H converts the simulated 4D mixing ratio fields into satellite-equivalent XCH_4 following the formulation described in Sect. 3.3.2. This involves applying the instrument-specific averaging kernels and a priori profiles, integrating along the vertical, and accounting for the sensitivity of each sensor (TIR or SWIR) to different parts of the atmospheric column.

https://doi.org/10.5194/egusphere-2025-5923
Preprint. Discussion started: 23 December 2025

3.3.2 Satellite-equivalent XCH_4 estimation using Averaging Kernels

The 4D mixing ratio fields simulated by LMDZ are converted into satellite-equivalent XCH_4 by applying the averaging kernels (AKs) and prior profiles from each retrieval, ensuring consistency with each satellite product.

GOSAT-TANSO

For GOSAT, the satellite-equivalent XCH_4 is obtained using Eq. (4), where $[CH_4]_i^{prior}$ is the prior mixing ratio in layer i, $[CH_4]_i^{mod}$ is the modeled mixing ratio interpolated to the retrieval levels, AK_i is the averaging kernel, and h_i is the pressure weighting function for layer i. For the GOSAT-NIES product, h_i is defined over 15 vertical layers, whereas for the GOSAT-Leicester product it is defined over 20 layers.

$$XCH_4 = \sum_{i=1}^{N_{lev}} \left[[CH_4]_i^{prior} + \left([CH_4]_i^{mod} - [CH_4]_i^{prior} \right) AK_i \right] h_i \quad (4)$$

The prior values and AKs are specific to each observation, allowing for a detailed and observation-consistent comparison between model and satellite retrievals. An illustration of the median averaging kernels is provided in Figure A2 in Appendix.

Metop-A IASI

For IASI-Metop-A, the satellite-equivalent XCH_4 is calculated using Eq. (5), where $[CH_4]_i^{mod}$ is the modeled mixing ratio at level i, AK_i is the averaging kernel, and w_i is the layer-dependent weighting function defined over 39 layers.

$$XCH_4 = \frac{\sum_{i=1}^{39} AK_i \, [CH_4]_i^{mod} \, w_i}{\sum_{i=1}^{39} AK_i \, w_i} \quad (5)$$

Sentinel-5P TROPOMI

For TROPOMI-WFMD, we apply the AK to the model profiles to compute the simulated XCH4 applying Eq. (6), h_i is defined over 20 vertical layer (Schneising, 2021).

$$XCH_4 = \sum_{i=1}^{N_{lev}} \left[[CH_4]_i^{prior} + \left([CH_4]_i^{mod} - [CH_4]_i^{prior} \right) AK_i \right] h_i \quad (6)$$

3.4 Error characterization and covariance design

As presented in Section 3.2, errors on the priors fluxes are represented in the $\mathbf{B}$ matrix, while errors on the observations are represented in the $\mathbf{R}$ matrix. The $\mathbf{B}$ matrix is decomposed into diagonal and off-diagonal terms. The diagonal contains the error variances, set to 100% of the squared maximum emissions within each grid cell and its eight neighbors for each month.

The off-diagonal terms describe the covariances between different cells, capturing dependencies among flux errors across space and time. Previous studies have generally adopted horizontal correlation lengths of 500–1000 km over land and 900–2000 km

https://doi.org/10.5194/egusphere-2025-5923
Preprint. Discussion started: 23 December 2025

over ocean, with temporal correlations of approximately one to three weeks (Cressot et al., 2016; Thompson et al., 2017; Wang et al., 2019). In the Global Methane Budget 2000–2020 (Saunois et al., 2025), models such as NIES-TM-FLEXPART, LMDZ-CIF, LMDZ-PYVAR, and CTE-CH_4 applied similar ranges: around 500 km over land and 500–1000 km over ocean, with temporal correlations of roughly 15–16 days (Maksyutov et al., 2021; Tsuruta et al., 2017; Thanwerdas et al., 2021; Wang et al., 2019; Zheng et al., 2018).

Building on this framework, we derived sector-specific spatial correlations using a semivariogram, which characterizes variance as a function of separation distance. A representative correlation length was selected for each flux category.

For temporal resolution, we used 10 days for more variable sources (agriculture, biomass burning, oil and gas, wetlands) and one month for smoother sectors. Temporal correlation scales reflect source dynamics: one month for agriculture, three months for coal, and six months for geological, oceanic, and waste emissions.

The temporal resolutions, horizontal correlation lengths, and temporal correlation scales applied to each sector are summarized in Table 1. Correlations decrease with increasing spatial and temporal separation, ensuring that the structure of $\mathbf{B}$ captures realistic flux variability.

	Agriculture	Biofuel	Biomass Burning	Coal	Geological	Oceans	Oil and Gas	Soil Sink	Termite	Waste	Wetland	Total
Horizontal Correlation (km)	500	500	600	500	1500	1500	500	1500	1500	500	700	500
Time Resolution	10 D	1 M	10 D	30 D	1 M	1 M	10 D	1 M	1 M	1 M	10 D	10 D
Time Correlation	1 M	2 M	1 M	3 M	6 M	6 M	1 M	2 M	2 M	6 M	1 M	1 M

Table 1. Spatial and temporal correlations lengths for an exponential decrease and time resolution of surface fluxes used to build the background error covariance matrix $\mathbf{B}$ (units: D = day, M = month).

The observation error covariance matrix $\mathbf{R}$ is represented only by its diagonal terms, which include both measurement (instrumental) errors and errors in the observation operator $\mathbf{H}$. Observation operator errors typically account for transport and chemistry uncertainties, representativeness errors (arising from the mismatch between model grid cells and point measurements), and aggregation errors (due to the limited resolution of the state vector).

For satellite observations, $\mathbf{R}$ includes the reported instrumental error plus an additional 10 ppb to account for model representation errors (Locatelli et al., 2015). This additional uncertainty follows the approach of Locatelli et al. (2015), who added a transport model error equivalent to about 1% of the observed values based on the tuning of error statistics by Cressot et al. (2014). For in-situ stations, a proxy for model error was estimated on a station- and year-specific basis from the Residual Standard Deviation (RSD) of the observations around a smooth fitted curve (Locatelli et al., 2013). This curve, constructed using three polynomial and eight harmonic coefficients, captures both the underlying trend and the seasonal cycle in the data (Masarie and Tans, 1995). The resulting RSD was then added to the instrumental error to represent the total uncertainty at each station and date.

https://doi.org/10.5194/egusphere-2025-5923
Preprint. Discussion started: 23 December 2025

To further ensure data quality, a direct simulation using the filtered dataset was performed, and the fit between observations and simulations was evaluated. Persistent outliers were identified as observations differing by more than three standard deviations from the simulations and subsequently removed.

A summary of the instrumental and model errors across all stations in 2019 is presented in Figure 4. While the mean instrumental error remains low (around 1.8 ppb), the combined contribution of instrumental and model errors leads to an average uncertainty of 23.97 ppb. Thus, the diagonal elements of R include both the instrumental error and the station-specific proxy for model error.

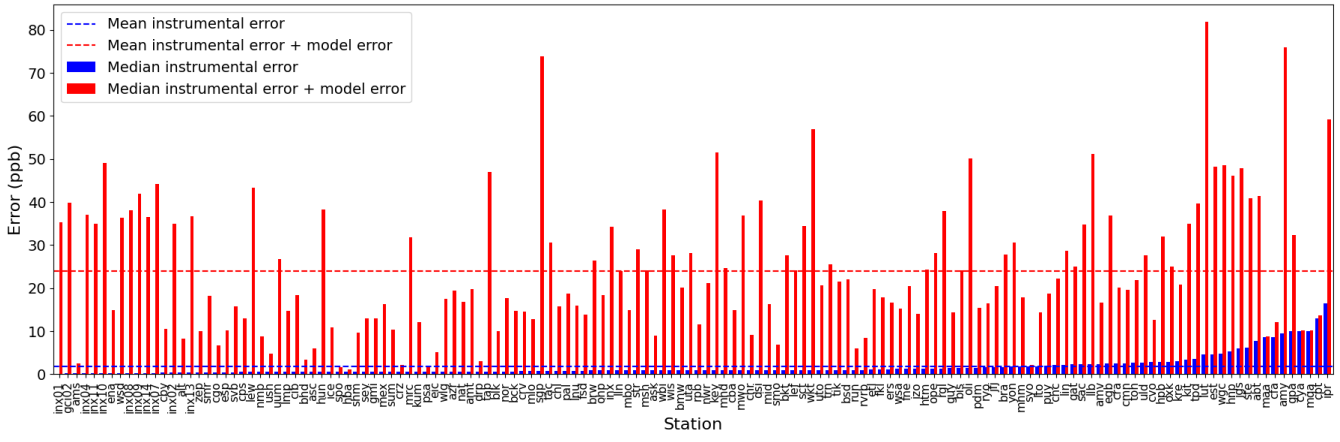

Figure 4. Median CH_4 mixing ratio measurement errors at in-situ stations during 2019. The stations are shown in ascending order according to the median instrumental error. Instrumental errors (blue bars) and total errors combining instrumental and model components (red bars) for the year 2019. Dashed lines represent the global mean values for each error type.

3.5 Sensitivity of the observing systems to the CH_4 surface fluxes

We evaluated the extent to which the emissions represented in the surface–flux control vector contribute to the signals measured by the observations, accounting for atmospheric dynamics and large-scale transport (Brasseur and Jacob, 2017).

For this purpose, we computed observation sensitivity to the fluxes, expressed as:

$$\mathbf{s} = \mathbf{H}^{\mathrm{T}}\,\delta\mathbf{y}^{*}$$

where $\mathbf{H}^{\mathrm{T}}$ denotes the adjoint of the linearized observation operator $\mathbf{H}$, obtained from the tangent-linear approximation of $\mathcal{H}$ around the background state. The vector $\delta\mathbf{y}^{*}$ denotes an arbitrary perturbation in the observation space, uniformly set to 1 in this study, to evaluate how a unit increase in the observations affects the estimated emissions. The absolute magnitude of the perturbation is arbitrary; the comparison of sensitivities between observing systems is independent of the chosen value, as the linearity ensures that relative responses are preserved

In CIF, the backward (or footprint) mode was employed to quantify the sensitivity of observed atmospheric mixing ratios, both from surface and satellite data, to global surface sources. The first step is to perform a forward mode calculation to obtain

https://doi.org/10.5194/egusphere-2025-5923
Preprint. Discussion started: 23 December 2025

a reference state of the atmosphere, which simulates the transport and chemistry of gases towards the receptor, in our case, the surface stations and the locations where the satellites provide observations. The outputs include, among other variables, the advection and diffusion fields, which are stored and later used in the backward calculations. The backward calculation is then performed for 2019, for each observing system, divided into three-month periods to focus on transport within shorter temporal scales. This approach better captures seasonal changes in circulation patterns and reduces temporal averaging, thus improving the accuracy of the sensitivity estimates compared with a full-year simulation. The quarterly footprints are then averaged to obtain the sensitivity of each observing system to the fluxes. Sensitivity results are illustrated and discussed in Fig. 7 and Sect. 4.1

3.6 Observing System Simulation Experiment set-ups

Observing System Simulation Experiments (OSSEs) are widely used to assess the potential value of planned or existing observation datasets (e.g., from satellite missions) for improving the estimation of greenhouse gas fluxes and understanding atmospheric processes (Brasseur and Jacob, 2017; Potier et al., 2022; Sicsik-Paré et al., 2025).

In this study, OSSEs were conducted under two configurations: (1) optimizing the total methane flux at the surface, and (2) optimizing fluxes disaggregated into eleven sectors (10 emissions + soil sink). Each configuration was tested for individual observing systems and for selected combinations, to evaluate their capability to constrain methane fluxes at the regional and sectoral scales. The observing systems include GOSAT-NIES, GOSAT-Leicester, IASI-MetOp-A, TROPOMI-WFMD, in-situ surface measurements, and combinations such as GOSAT-NIES + in-situ and GOSAT-Leicester + in-situ.

Figure 5 presents the overall OSSE framework. The process begins with the definition of a "true" state, which combines meteorological data, prescribed oxidant mixing ratios, prior fluxes, and initial conditions.

A forward simulation is subsequently performed using the LMDZ general circulation model coupled with the simplified atmospheric chemistry module SACS, producing synthetic 4D mixing ratio fields that represent the “perfect” atmosphere. These fields are then sampled for in-situ stations and converted to mixing ratio XCH_4 using the observation operator ($\mathcal{H}$), which applies instrument-specific averaging kernels, a priori profiles, and vertical integration as described in Sect. 3.3.1. In this way, both satellite and in-situ observations are incorporated into the OSSE framework, as illustrated in Fig. 5.

The inversion is carried out within a 4D-Var framework using 10 independent ensemble members. Each member employs perturbed priors generated via a Monte Carlo approach and adjusts them to fit the synthetic observations through a cost function minimization process. During inversion, the observational error covariance matrix ($\mathbf{R}$) — described in Sect. 3.4 — and the prior flux error covariance matrix ($\mathbf{B}$) — detailed in Sect. 3.4 and Fig. 1 — are explicitly accounted for.

Finally, the posterior fluxes are compared with the true reference state at multiple spatial and temporal scales (global, regional, and sectorial) to evaluate the inversion performance and quantify the impact of each observing system configuration (see Sect. 3.7).

https://doi.org/10.5194/egusphere-2025-5923
Preprint. Discussion started: 23 December 2025

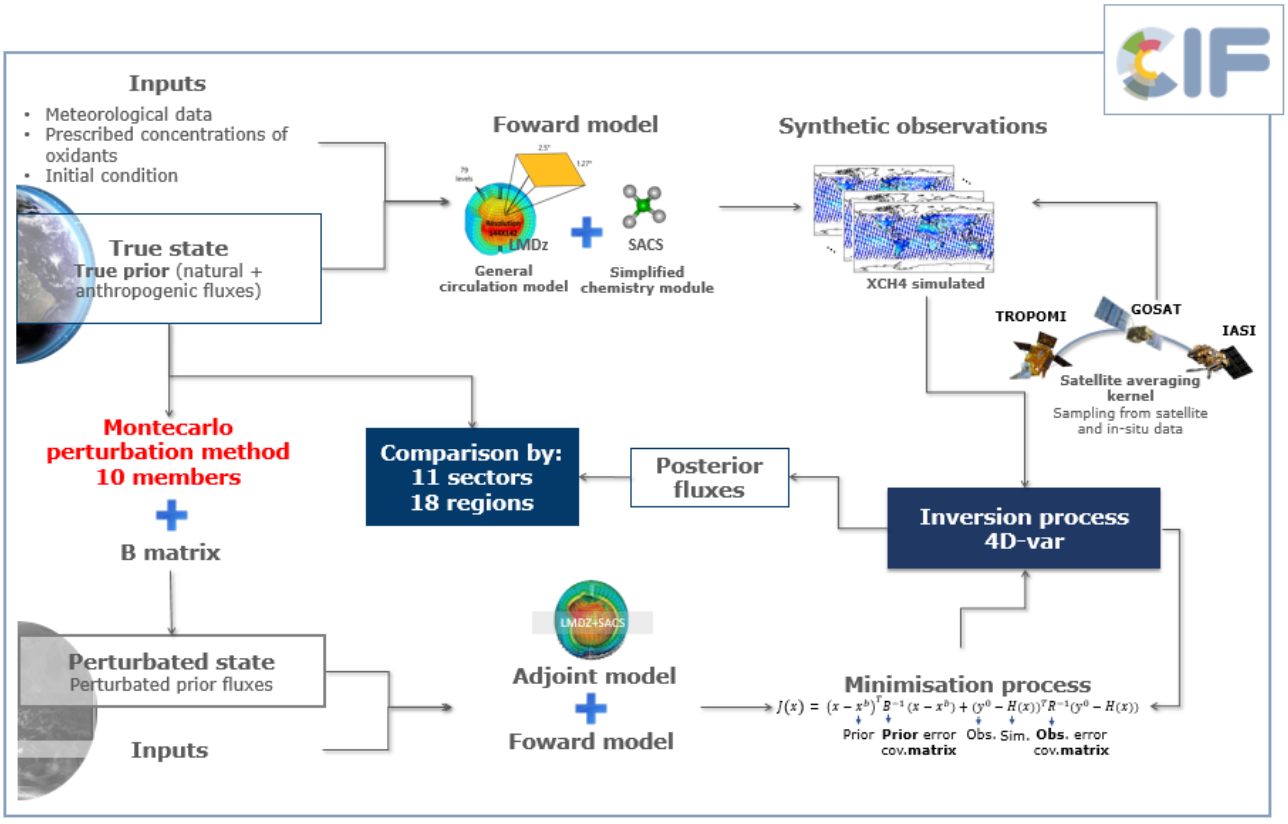

Figure 5. Schematic of the methodology used to perform an OSSE for atmospheric inversion in the CIF with the LMDZ model.

3.7 Assessment of Inversion Performance and Uncertainty Reduction

Relative Flux Improvement Metric (M)

The OSSE results are analyzed at the regional scale by dividing the domain into 18 regions (see Figure 2). A performance metric, $\mathbf{M}$, is defined for each region, observing system and sector, as the ratio of the posterior to true distance to the prior to true distance, quantifying the improvement of the posterior fluxes over the prior.

For each region $\mathbf{r}$ and month $\mathbf{t}$, the regional fluxes are first aggregated over region and emission sectors. The monthly performance indicator $\mathcal{L}_{r,t}$ is then defined as:

$$\mathcal{L}_{r,t} = \log\left(\left|\frac{\mathrm{Post}_{r,t} - \mathrm{True}_{r,t}}{\mathrm{Prior}_{r,t} - \mathrm{True}_{r,t}}\right|\right), \tag{7}$$

where $\mathrm{Post}_{r,t}$, $\mathrm{Prior}_{r,t}$, and $\mathrm{True}_{r,t}$ represent the regionally aggregated posterior, prior, and true fluxes, respectively.

https://doi.org/10.5194/egusphere-2025-5923
Preprint. Discussion started: 23 December 2025

The annual regional metric $\mathcal{L}_r$ is obtained by averaging $\mathcal{L}_{r,t}$ over all months:

$$\mathcal{L}_r = \frac{1}{N_t} \sum_{t=1}^{N_t} \mathcal{L}_{r,t}, \tag{8}$$

where N_t is the number of months in the analyzed year (12).

Finally, the overall regional performance indicator M is expressed as:

$$M = \left(\exp(\overline{\mathcal{L}_r}) - 1\right) \times 100, \tag{9}$$

where $\overline{\mathcal{L}_r}$ denotes the mean value of $\mathcal{L}_r$ across the ensemble of ten inversion realizations.

Negative values of $\mathbf{M}$ indicate that the posterior fluxes are closer to the true fluxes than the prior, reflecting a positive contribution of the observing system, whereas positive values indicate that the posterior fluxes fail to improve upon the prior in reproducing the truth (darker blue in Figure 6).

Uncertainty Reduction (UR)

UR quantifies the decrease in the spread of the estimated fluxes after the inversion, relative to the prior ensemble variability. For each region and month, the posterior and prior fluxes are first aggregated spatially over all regions and sectors. Then, for each month, the standard deviation across the 10 ensemble members is computed separately for the prior and posterior fluxes.

The monthly uncertainty reduction is defined as:

$$UR_r, t = \left(1 - \frac{\sigma_{r,t}^{\text{post}}}{\sigma_{r,t}^{\text{prior}}}\right) \times 100, \tag{10}$$

where $\sigma_{r,t}^{\text{post}}$ and $\sigma_{r,t}^{\text{prior}}$ denote the standard deviations of the posterior and prior fluxes, respectively, computed across the 10 ensemble members for each region r and month t. The monthly UR values are then averaged over the t = 12 months to obtain an annual regional mean uncertainty reduction:

$$UR_r = \frac{1}{N_t} \sum_{t=1}^{N_t} UR_{r,t}, \tag{11}$$

Higher values of UR indicate a larger reduction in the ensemble spread, and thus a stronger constraint of the inversion system on the estimated fluxes.

Relative Sectoral Uncertainty Reduction ($RSUR$)

https://doi.org/10.5194/egusphere-2025-5923
Preprint. Discussion started: 23 December 2025

To assess the relative contribution of each emission sector to the overall reduction of uncertainty, we define the ($RSUR$) as the ratio between the fractional contribution of a given sector to the total uncertainty reduction and its fractional contribution to the total prior emissions, minus one to center the metric around zero:

$$RSUR = \frac{\left(\frac{UR_{\text{sector}}}{UR_{\text{total}}}\right)}{\left(\frac{E_{\text{sector}}}{E_{\text{total}}}\right)} - 1, \tag{12}$$

where UR_{sector} and UR_{total} represent the uncertainty reductions for a specific sector and for all sectors combined, respectively, while E_{sector} and E_{total} denote the corresponding prior emissions.

A value of $RSUR$ close to zero indicates proportionality between the sectoral contribution to the total uncertainty reduction and its share in total prior emissions. Positive (negative) $RSUR$ values indicate that the sector contributes more (less) to the total uncertainty reduction than expected from its emission share.

4 Results

The results of the global methane OSSEs are presented in three parts. First, in Section 4.1, we examine the regional-scale potential of individual observing systems, highlighting their observation density, errors, sensitivities, prior flux contributions, and uncertainty reduction (Figures 6, 7). Next, in Section 4.2 we explore the complementarity between systems using zonal evaluation by regions and latitude bands, focusing on uncertainty reduction and performance metrics (Figures 8). Finally, in Section 4.3 we assess their ability to constrain sectoral fluxes through regional and sectoral uncertainty reductions and flux repartition (Figures 9 and 10). This structure provides a consistent framework to evaluate and compare observing systems across regional, latitudinal, and sectoral scales.

4.1 Evaluating the potential of individual observing systems to retrieve methane flux at the regional scale

Figure 6 shows the density of observations, the associated median observation errors (instrumental plus model-related), the sensitivity of the observations to surface methane fluxes (with pixel-scale sensitivities illustrated in Figure 7), the performance of M, and the resulting uncertainty reduction UR. In addition, prior fluxes are represented regionally in terms of their total flux contribution. This comprehensive view is intended to provide, at a glance, all the elements needed to evaluate and compare the ability of each observing system to constrain regional methane fluxes.

The coverage of surface measurements — densest in the USA, Canada, Europe, and Korea–Japan (ranging between 100 and 1000 observations km^{-2}) — results in the highest sensitivities for this observing system, reaching values on the order of 10^5 ppm $(\text{kg}\,\text{m}^{-2}\,\text{s}^{-1})^{-1}$ km^{-2}.

https://doi.org/10.5194/egusphere-2025-5923
Preprint. Discussion started: 23 December 2025

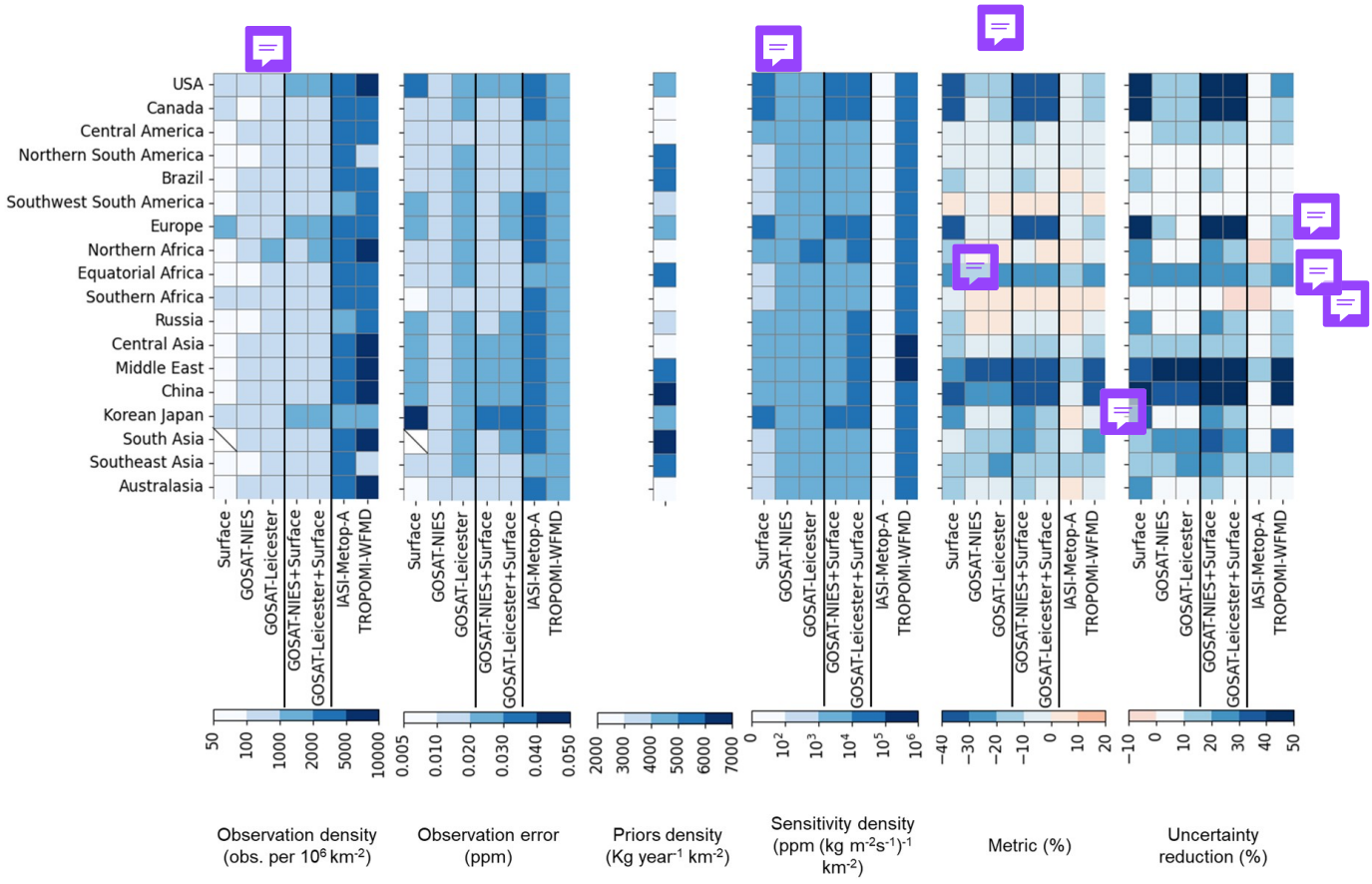

Figure 6. Regional synthesis of the OSSE results by observing system, including observation density, errors, sensitivity to fluxes, prior density, performance M, and UR. Observation count, prior fluxes, and sensitivities are normalized by the surface area of each region (km^2) to allow for meaningful comparison across regions. The distribution of the 18 regions is shown in Fig. 2. The performance metric quantifies the ability of each observing system to improve posterior flux estimates relative to perturbed priors, expressed as a percentage. A more negative value (darker blue) indicates that the posterior is closer to the target flux. Overall, the darker blue corresponds to the highest and most desirable values to achieve

In regions with an observational density below 100 observations $km^{-2}x10^6$, sensitivities are about one order of magnitude higher in the Northern Hemisphere than in the Southern Hemisphere. For instance, Central America, Northern Africa, the Middle East, and parts of Asia show higher sensitivities compared to South America, Australasia, and Southern Asia. This pattern can be explained by a stronger influence of the in-situ network localized mainly in the Northern Hemisphere (Fig. 2).

Regions with the highest sensitivities—namely the USA, Canada, Europe, and Korea-Japan—also show the best performance of the surface observation network. In these areas, posterior flux estimates closely approach the target, with M values above 20%. Some regions, such as China, have low sensitivity but very high flux densities (≈7000 kg yr^{-1} km^{-2}). In these cases, posterior flux estimates may appear improved; however, this apparent improvement reflects the fact that the large flux signals are near the system's detection threshold, rather than a true enhancement of constraints. Conversely, regions with M values

https://doi.org/10.5194/egusphere-2025-5923
Preprint. Discussion started: 23 December 2025

below -20% generally correspond to areas where uncertainty reductions exceed 20%, indicating that stronger observational constraints lead to more accurate flux estimates. Overall, the spatial patterns of M and uncertainty reductions are closely linked ($r^2 = 0.94$), clearly illustrating how the observations contribute to constraining regional methane fluxes (Figure B1 in Appendix.

In summary, the regions that are better constrained by in-situ surface observations are mostly located in the Northern Hemisphere, where the density of measurements is high and fluxes are relatively large. In contrast, Southern Hemisphere regions such as South America and southern Africa show both M values and uncertainty reductions close to zero, highlighting blind spots of the global surface network where the system's sensitivity to surface fluxes remains very low.

Focusing on the GOSAT products from NIES and the University of Leicester, both systems provide similar regional sensitivities to surface fluxes, as illustrated in Fig. 6, with observation densities of the same order of magnitude (approximately 10^2–10^3 observations per 10^6 km^2). The GOSAT-Leicester product, however, delivers roughly three times more observations per pixel than GOSAT-NIES (Fig. 1), albeit with a higher median retrieval error of about 0.02 ppm, which includes both instrumental and proxy model error. At the pixel resolution as shown in Fig. 7, Leicester exhibits higher sensitivities in the tropics; however, both products show similar performance at the regional scale (Fig. 6).

Using GOSAT, M and UR are generally consistent, with the USA, Equatorial Africa, Central Asia, and the Middle East showing absolute values between 10–40% in both M and UR. The Middle East stands out with a 40% uncertainty reduction in a region characterized by a high flux density of approximately 5000 kg yr^{-1} km^{-2}. Some regional differences are evident: the GOSAT-Leicester inversion provides better constraints over Canada and Southeast Asia than GOSAT-NIES, while slightly weaker performance of GOSAT-Leicester is observed over southwestern South America. Regions in the Southern Hemisphere, such as Central and South America and southern Africa, remain poorly constrained despite increased GOSAT coverage. Compared with the surface network, this highlights persistent blind spots in the global observing systems.

Overall, both GOSAT products show broadly similar performance. The GOSAT-Leicester dataset provides higher observation density, whereas GOSAT-NIES offers lower observational errors, which may be advantageous for computational efficiency. Although GOSAT observations enhance coverage in the Southern Hemisphere, they do not outperform the constraints achieved using in-situ surface measurements. Surface and satellite data together effectively constrain high-flux regions, such as the USA, Equatorial Africa, the Middle East, and China. In contrast, some regions, including South America, exhibit only limited reductions in posterior uncertainty despite available observations, indicating that a high coverage alone does not guarantee strong flux constraints.

https://doi.org/10.5194/egusphere-2025-5923
Preprint. Discussion started: 23 December 2025

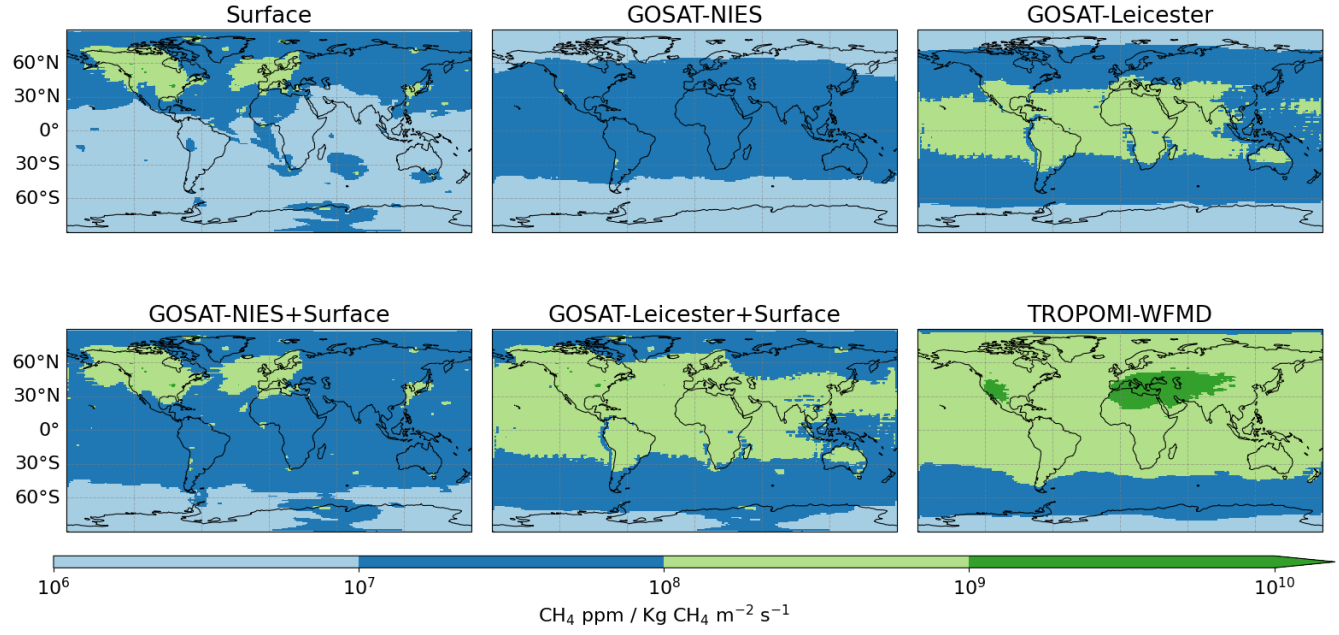

Figure 7. Quarterly-averaged sensitivity of the observing systems to methane fluxes. Sensitivities are computed for each three-month period in 2019 and then averaged to represent the global sensitivity of each system.

TROPOMI-WFMD provides the highest observation density, reaching up to 10,000 observations $km^{-2} \times 10^6$ in regions such as the USA, Northern Africa, and Central Asia. This is about two orders of magnitude higher than most other systems, with the exception of IASI-Metop-A. As a result, TROPOMI-WFMD exhibits the strongest sensitivities to surface fluxes, comparable to in-situ measurements in regions such as the USA, Canada, and Korea-Japan. On average, sensitivities are roughly one order of magnitude higher than GOSAT, and can reach up to two orders of magnitude higher in Central Asia and the Middle East.

Despite its high sensitivity and extensive global coverage, TROPOMI-WFMD does not exhibit substantially superior performance in recovering fluxes (M), nor in reducing posterior uncertainties, compared to the GOSAT products. Slight improvements of about 10% are observed in well-constrained regions such as the USA, Europe, and South Asia. However, in the Southern Hemisphere, particularly in southwestern South America and southern Africa, posterior flux estimates remain poorly constrained despite the presence of observational data. This limited constraint arises from a combination of factors: relatively low local sensitivity of the system, weaker CH_4 flux signals in these regions, representativeness error due to the mismatch between the model resolution and the spatial footprint of the observations, and the finite precision of the observations themselves as represented in the diagonal elements of the observation error covariance matrix R. Consequently, high observational coverage alone does not guarantee substantial uncertainty reduction, as the strength of flux constraints also depends on the local effectiveness of the observational system, including both measurement precision and representativeness.

Finally, IASI-Metop-A provides a high observation density, ranging between 2,000 and 5,000 observations km^{-2}, but it also exhibits the highest associated error among the remote-sensing systems, with a median value of 0.04 ppm. Its regional

https://doi.org/10.5194/egusphere-2025-5923
Preprint. Discussion started: 23 December 2025

sensitivity is nearly 0 ppm kg m^{-2} s^{-1}), which arises from the fact that, in the thermal infrared (TIR) band, it is not capable of detecting changes in methane concentrations near the surface. As shown in the averaging kernel (Figure A2 in Appendix), the CH_4 product is mainly sensitive to the atmospheric layer spanning approximately 50–500 hPa, with a peak sensitivity around 150 hPa between 50°N and 35°S, and around 300 hPa at other latitudes. Consequently, its ability to recover the target metric and to reduce uncertainty is very small. Only in Equatorial Africa, the Middle East, and Southeast Asia does the M value exceed 10%, with uncertainty reductions slightly above 10%.

In summary, using individual observing systems, the OSSE reveals that high-emission regions such as the USA, China, Equatorial Africa, and the Middle East are effectively constrained by both in situ and satellite-based observations. M and UR values in these regions range approximately 10–40%, indicating substantial constraint on posterior flux estimates. However, persistent challenges remain in the Southern Hemisphere. In northern South America and Brazil, methane fluxes are high (≈5000–6000 kg yr^{-1} km^{-2}), while in southern Africa they are somewhat lower (≈2000–3000 kg yr^{-1} km^{-2}). Despite these substantial emissions, posterior estimates remain poorly constrained across all observing systems, by discussing regions where observational coverage does not translate into strong flux constraints.

4.2 Complementarity between in-situ and satellite products across region

The combination of in-situ and GOSAT observations improves performance relative to surface-only assimilation, as shown in the M and UR columns of Figure 6. Regions that were already well constrained by surface measurements—such as the USA, Canada, Europe, and China with M improvements of –30% to –40% and UR of 40–50%), retain their strong performance under both GOSAT+Surface combinations.

Additional improvements relative to the surface-only assimilation are observed with GOSAT–NIES+Surface (GN+S) in Central America (-10% to -20%), the Middle East (-20% to -30%), and South Asia (0% to -30%), where both M and UR indicate stronger constraints. Similarly, GOSAT–Leicester+Surface (GL+S) shows an improvement in South Asia, with M and UR increasing from 0% to -20% compared to surface-only observations.

Conversely, slight degradations appear in Northern and Southern Africa, where M and UR decrease (e.g., from -10% to 0%) when GOSAT data are added to the in-situ network. This apparent decline does not necessarily reflect poorer performance of the satellite data. Rather, it likely results from the lack of surface reference sites in these regions, which prevents improvements from being captured by surface-based metrics. In addition, GOSAT retrievals over arid areas are often affected by higher surface reflectance and limited data coverage, which can increase observation noise and reduce their constraining power. Nevertheless, improvements in regions with few in-situ observations can still arise through the spatial propagation of observational information via atmospheric transport and prior error correlations within the inversion framework.

Between the two combinations, GN+S outperforms GL+S over Brazil, Northern Africa, Russia, Korea–Japan, and Australasia. These differences can be partly explained by the trade-off between observation density and associated errors: while GOSAT-Leicester provides a higher number of observations, GOSAT-NIES offers lower errors, which appears to result in stronger constraints when combined with the in-situ network.

https://doi.org/10.5194/egusphere-2025-5923
Preprint. Discussion started: 23 December 2025

When comparing TROPOMI-WFMD with the GOSAT+surface combinations, TROPOMI generally exhibits higher sensitivities to surface fluxes, roughly one order of magnitude greater than GOSAT–NIES and similar to GOSAT–Leicester across regions between 60°N and 30°S. However, in terms of flux recovery (M) and UR, TROPOMI only approaches the performance of the GOSAT+surface combinations in the Middle East and China, achieving, for example, $UR \approx 40\%$ and $M \approx -40\%$.

In most other regions, the GOSAT+surface system outperforms TROPOMI, despite TROPOMI's dense temporal sampling. This reflects the complementary strengths of surface measurements and GOSAT columns in our OSSE: surface sites provide continuous, high-signal observations near the surface, anchoring the methane background, while GOSAT adds vertically-integrated column information. By contrast, TROPOMI's column measurements are more diluted vertically, limiting their effective constraint on fluxes under the assumed error structures.

To further assess the complementarity between the surface network and satellite instruments, we evaluated their performance for total methane fluxes across latitudinal bands (Figure 8 for M and UR). Between 90°N and 60°N, surface-based inversions yield $M \approx -20\%$ and $UR \approx 18\%$, suggesting a good overall capability to constrain the total flux. Their combinations with GOSAT products produce slightly lower values, reflecting marginally weaker constraints in these high-latitude regions. In contrast, inversions relying solely on GOSAT or IASI-Metop-A provide almost no improvement in total flux estimates at these latitudes, as data filtering effectively removed most satellite observations (Figure 1).

https://doi.org/10.5194/egusphere-2025-5923
Preprint. Discussion started: 23 December 2025

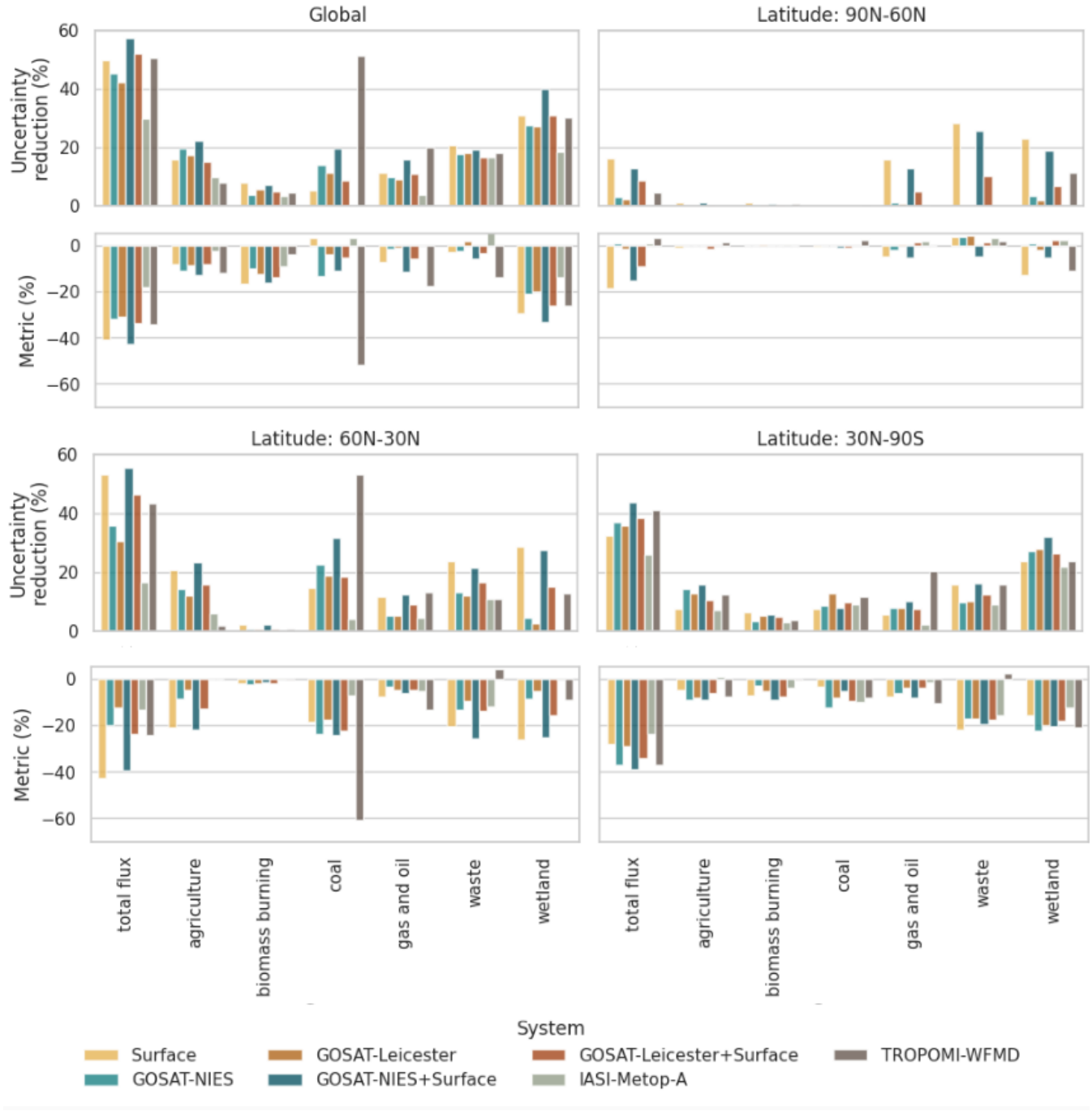

Figure 8. M and UR for both cases: total flux and separated fluxes by latitude bands.

In the 60°N–30°N latitudinal band, GN+S inversions provide the strongest performance, achieving a M value of approximately -40%, and UR above 50% which are about twice that of GOSAT–NIES and four times that of GOSAT–Leicester alone,

https://doi.org/10.5194/egusphere-2025-5923
Preprint. Discussion started: 23 December 2025

illustrating the dominant role of surface observation-based in this. Result reflecting the high density and favorable location of surface stations, about 60% of which are situated within this latitude range. Combined systems closely follow the surface network, particularly GN+S, which also outperforms both individual GOSAT products and GL+S in terms of uncertainty reduction.

South of 30°N, GN+S delivers the best performance, reaching a M value close to -40%, comparable to both GOSAT–NIES and TROPOMI-WFMD. Uncertainty reduction is similar across most systems (35%), with the exception of IASI, while GN+S shows a slight advantage. The complementarity of GOSAT products with in-situ observations becomes evident in this latitude band, where observation coverage is sparser and satellite data provide a valuable contribution.

At the global scale, GN+S consistently delivers the best performance, reaching nearly –40% in the M and about 40% in UR, thus outperforming all other observing systems. Although TROPOMI-WFMD provides daily global coverage, except in regions persistently affected by clouds, its higher observational errors and stronger data filtering reduce its effective contribution to flux constraints. In contrast, the GN+S combination proves to be an efficient alternative, extending the spatial coverage of the in-situ network while maintaining high precision, owing to the low observational errors of GOSAT–NIES.

In summary, the complementarity between in-situ and satellite systems is substantial, particularly in regions with sparse observational coverage. The best-performing configurations are not necessarily those with the highest observation density, but those that achieve a balance between coverage and precision. Nevertheless, persistent blind spots remain—most notably in northern South America—where cloud cover severely limits SWIR retrievals. This highlights the urgent need to reinforce the in-situ network in the tropics and to obtain satellite retrievals from partial cloud cover using for instance lidar instruments such as the future MERLIN mission (Ehret et al., 2017) to ensure more robust global methane flux estimation.

4.3 Potential of a single observing system to retrieve sectoral fluxes

The final step of our analysis evaluates the extent to which individual observing systems can constrain methane fluxes by sector. Figure 9 summarizes the uncertainty reduction achieved by the different observing systems when optimizing both the total flux (first columns, corresponding to Figure 6) and individual sectors. For this analysis, we focus on the six sectors contributing the most to global methane emissions, agriculture, biomass burning, coal, gas and oil, waste and wetland, as illustrated in Figure 3. Additionally, we perform a brief analysis of the performance of the satellite systems in constraining sectoral fluxes by latitudinal bands. Finally, we examine the relationship between the sectoral constraint and the sector contribution to the total regional flux, as represented in Figure 10.

Agriculture shows the highest UR value in Europe, where this sector accounts for 36% of regional emissions : UR value up to 35% when assimilating the GN+S combination. In South Asia, UR values for the agriculture sector reaches 15–20% with TROPOMI-WFMD and both GOSAT products, and 25% with GN+S, despite the challenge to measure methane in this equatorial region (Figure A3). In contrast, China exhibits weaker UR value (15%), even though agriculture represents 29% of its national emissions.

https://doi.org/10.5194/egusphere-2025-5923
Preprint. Discussion started: 23 December 2025

Coal is the dominant sector in China, accounting for 32% of national emissions and 54% of global coal emissions. UR value for the coal sector exceeds 15% for all satellite systems except IASI-Metop-A, with GN+S and TROPOMI-WFMD reaching 40–50%. In Southeast Asia, coal contributes approximately 10% of emissions, with UR values around 15% only.

Oil and gas sector is particularly prominent in the Middle East. This sector accounts for 65% of regional emissions and 24% of global oil and gas emissions. Over the Middle East, TROPOMI-WFMD achieves a UR value of 35%, whereas the GOSAT products and their combinations with in situ data achieve about 15% of uncertainty reduction. In North America, in situ observations constraints for the oil and gas sector, with UR values ranging from 20% to 25% in the USA and Canada. In contrast, other regions show no uncertainty reduction, even where sectoral contributions are substantial, for instance, in Russia, where oil and gas account for about 22% of total emissions.

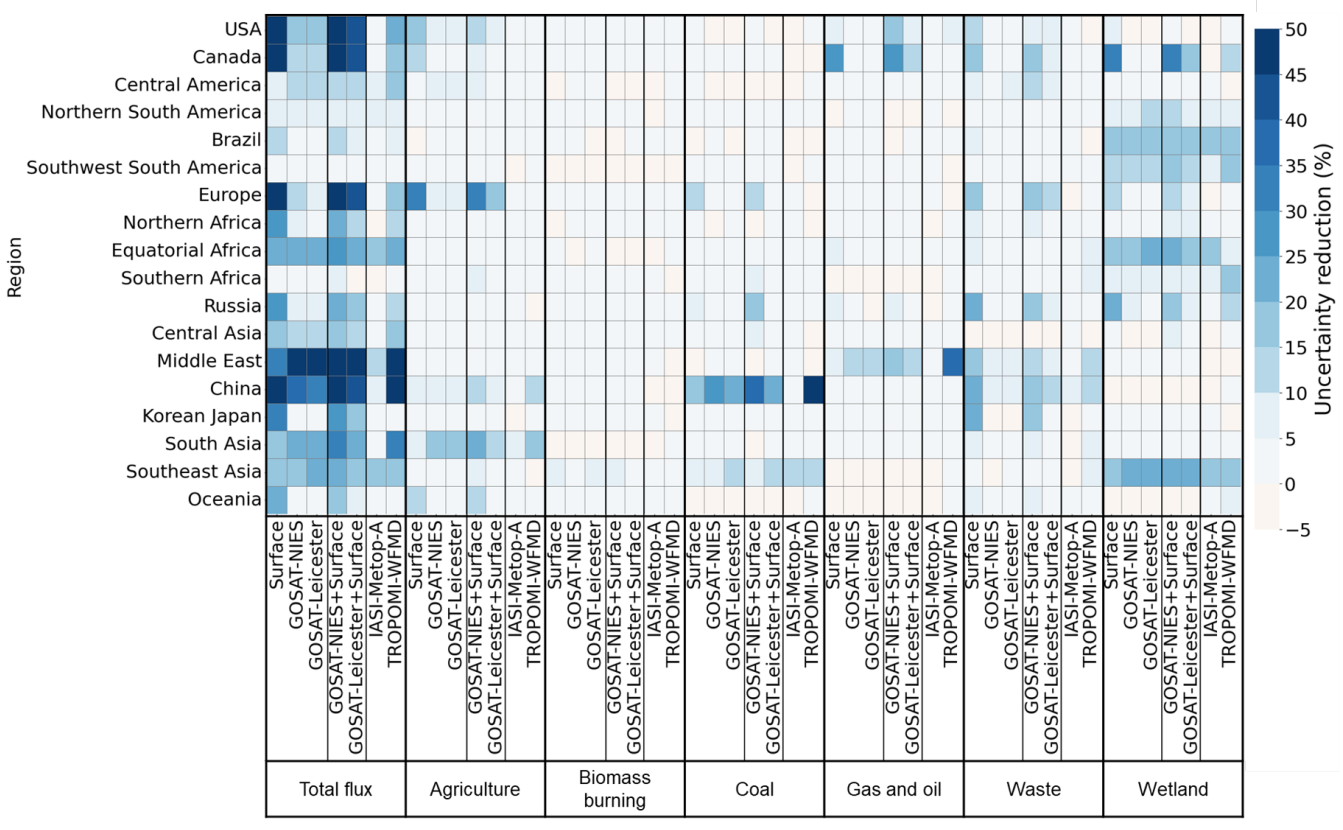

Figure 9. UR for optimization experiments targeting total flux and individual sectors. Results are shown for seven observing systems and evaluated across 18 regions trough OSSEs.

Waste sector shows only moderate constraints, with UR values of about 15–20% in regions such as Europe, Canada, Russia, China, the Middle East, and Korea–Japan when assimilating surface observations. Using TROPOMI-WFMD, uncertainty reduction reaches around 15% in the Middle East and China, but remains below 10% elsewhere. This sector is globally widespread, with China contributing roughly 20% of global waste emissions, while Europe and South Asia each account for

https://doi.org/10.5194/egusphere-2025-5923
Preprint. Discussion started: 23 December 2025

about 11%. Despite their significant contributions, these regions remain only moderately constrained, reflecting the spatially heterogeneous and widespread distribution of numerous point sources of waste-related methane emissions.

Wetland emissions despite their diffuse spatial distribution—exhibit notable UR value in several regions. In Canada, surface observations achieve an UR value of 35%. Substantial reductions are also observed for Brazil, southwestern South America, equatorial Africa, Russia, and Southeast Asia, with UR value ranging from 10% to 25%. This stronger performance relative to the waste sector can be attributed to the larger global prior flux from wetlands ($181\,\mathrm{Tg\,yr^{-1}}$) compared to the waste sector ($98\,\mathrm{Tg\,yr^{-1}}$)), as shown in Figure A4. Regionally, wetlands dominate methane emissions in Brazil (48%), equatorial Africa (46%), Russia (41%), and Southeast Asia (37%), whereas waste contributes less than 10% in these same regions. In high-latitude regions such as Canada and Russia, surface observations provide the strongest constraints, while in tropical and mid-latitude bands both in-situ and satellite-based systems show comparable performance. The stronger wetland signal thus provides greater sensitivity and a more effective constraint on flux estimates.

Biomass burning does not exhibit high UR value in any region, consistent with its limited contribution to total emissions (<10%, and in some regions below 1%). Unlike diffuse agricultural sources, biomass burning is characterized by localized and episodic events. Larger uncertainty reductions would therefore be expected in tropical regions, where major fire events occur; however, this is not observed.

Overall, the sectoral analysis highlights that high-emission sectors—such as agriculture in South Asia, coal in China, and oil and gas in the Middle East—are effectively constrained by combinations of surface and satellite observations, particularly GN+S and TROPOMI-WFMD. In contrast, sectors characterized by diffuse or relatively low emissions, such as biomass burning and waste in certain regions, remain poorly constrained. These findings underscore the importance of integrating complementary observing systems to maximize sectoral flux constraints, while persistent observational gaps in regions such as equatorial South America emphasize the urgent need to expand in-situ coverage and to take better advantage of upcoming spaceborne lidar missions offering high vertical resolution (Bousquet et al., 2018).

A likely explanation lies in the limitations of the LMDZ model, which does not explicitly represent pyro-convection processes in its current version (LMDZ6A; Hourdin et al. (2020)), leading to an underestimation of vertical transport of fire plumes. Such processes are generally better captured in higher-resolution models, which could provide more reliable constraints for this sector in future studies.

https://doi.org/10.5194/egusphere-2025-5923
Preprint. Discussion started: 23 December 2025

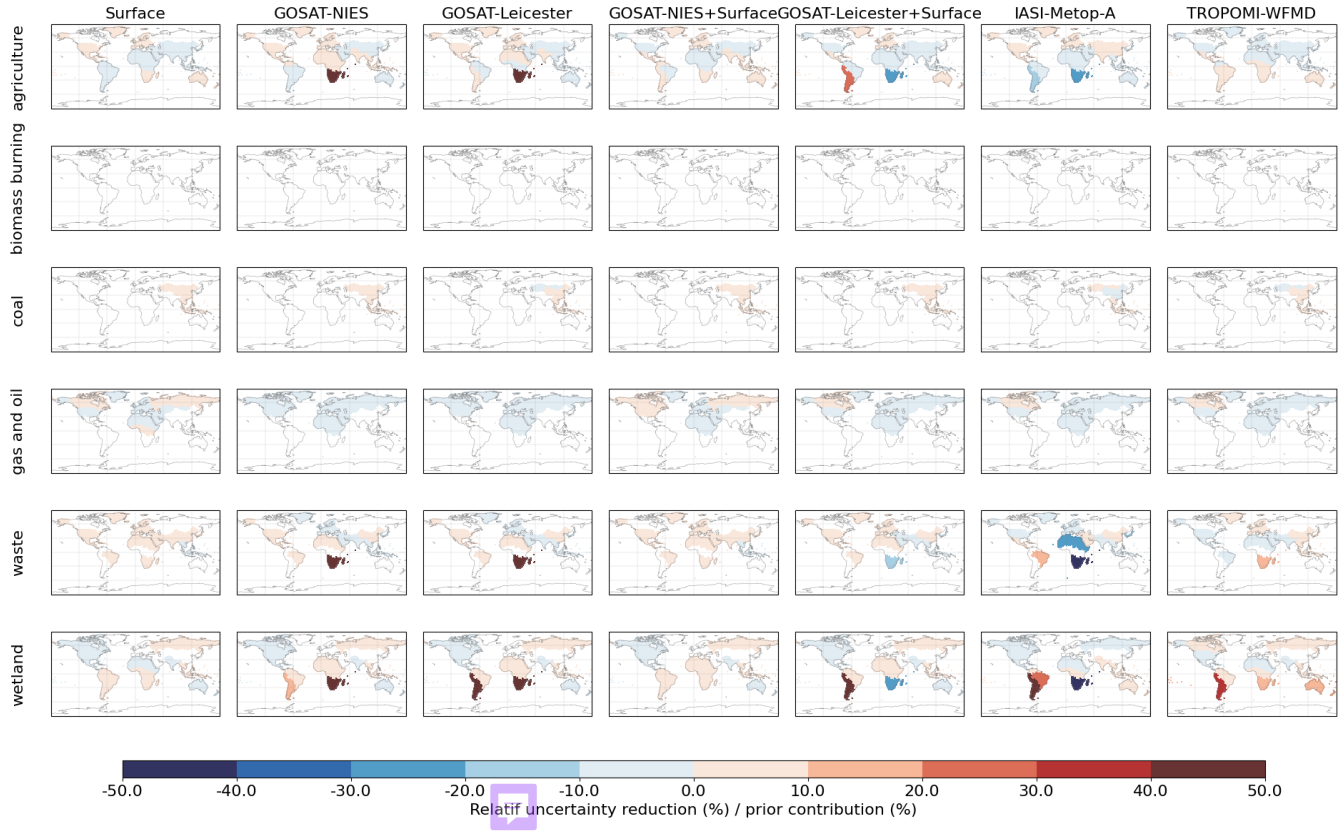

Figure 10. Relative Sectoral Uncertainty Reduction ($RSUR$, %) for six methane emission sectors across seven observing system configurations. $RSUR$ is defined as the ratio between relative uncertainty reduction (sector UR / total UR) and the sectoral contribution to the prior emissions (sector prior / total prior, see Section 3.7). A minimum emission contribution threshold of 10% was applied 10%. Values close to zero indicate proportionality between UR and emissions, while positive (negative) values denote that the sector contributes more (less) to uncertainty reduction than expected from its emission share. Rows correspond to emission sectors and columns to observing systems or system combinations.

Figure 10 presents the Relative Sectoral Uncertainty Reduction ($RSUR$), expressed as a percentage, for six major methane emission sectors across seven observing system configurations. $RSUR$ is defined in Equation 12 in Section 3.7 as the ratio between the sectoral contribution to the total uncertainty reduction and its share in the total prior emissions, centered around zero. A value close to zero indicates proportionality between the sectoral contributions to uncertainty reduction and prior emissions, whereas positive (negative) values denote that a sector contributes more (less) to uncertainty reduction than expected from its emission share. An equivalent analysis at the country scale is provided in the Appendix (Fig. B3).

Overall, $RSUR$ values are generally close to zero, indicating that the contribution of each sector to the total uncertainty reduction is roughly proportional to its share in total emissions, consistent with the scatterplots presented in the Appendix (Fig. B4). However, for sectors such as agriculture, waste, and wetlands, regions in the Southern Hemisphere—particularly

https://doi.org/10.5194/egusphere-2025-5923
Preprint. Discussion started: 23 December 2025

southern Africa and southwestern South America—show more positive (red) $RSUR$ values for GOSAT and TROPOMI-WFMD, suggesting a relatively larger uncertainty reduction compared to their emission contribution. Biomass burning is not shown, as its relative contribution remains below 10% in all regions and was thus filtered out. For the coal sector, only regions where its contribution exceeds 10% are displayed, corresponding mainly to China and Southeast Asia, where $RSUR$ values are positive, indicating stronger-than-expected constraints relative to their emission share.

Overall, these results highlight that sectoral uncertainty reduction is mostly but not solely determined by emission contribution. Observational system configuration and regional coverage play a critical role, with integrated surface–satellite networks generally providing more consistent improvements across sectors. Sectors, such as agriculture and oil and gas, having UR proportional to or exceeding their emission share, while others, such as waste and biomass burning, remain relatively poorly constrained. These findings emphasize the importance of combining complementary observing systems (e.g., in-situ and satellite) and targeted observational strategies to optimize sector-specific uncertainty reduction.

5 Discussion

5.1 Scope, sources of uncertainty, and limitations in OSSE

OSSEs are powerful tools to assess the potential of observing systems, but they do not reproduce the full complexity of the real atmosphere. Beyond this complexity, there are also inherent uncertainties associated with the tools themselves, including both the model and the observations and also their fusion. In our framework, the atmosphere is "perfect": there are no transport biases, no errors in OH or other sinks, no systematic biases in the observations, and the initial conditions are assumed to be exact. This idealization is important to keep in mind, since OH represents a major source of uncertainty in top-down CH_4 inversions (contributing about 17% to global methane emissions; Zhao et al. (2020)), while transport model errors contribute about 5% (Locatelli et al., 2013), and biases in satellite-based XCH_4 retrievals remain, impacting inversion comparisons and results (Sicsik-Paré et al., 2025). As a result, the uncertainty estimates from OSSEs should be considered a lower bound, not representative of the full range of real-world uncertainties (Masutani et al., 2010).

Another limitation is the temporal scope: we only analyzed one year and reported a single annual uncertainty reduction value. While this provides a representative snapshot, it does not capture intra-annual variability, inter-annual changes in transport, chemistry, or emissions, nor exceptional events such as large fires. This analysis estimates the system's ability to "recover" annual fluxes over a single year, rather than capturing intra-annual variations or longer-term trends (which the system might be better able to detect), due to computational constraints.

Finally, the uncertainty reduction reported here reflects the combined effect of prior perfectly known and observational uncertainties. This makes it difficult to disentangle the specific contribution of the observing system itself and highlights the need for cautious interpretation when extrapolating OSSE results to real-world applications.

https://doi.org/10.5194/egusphere-2025-5923
Preprint. Discussion started: 23 December 2025

5.2 Limitations from model resolution, vertical representation, and observational representativeness

One important limitation of our inversions is the mismatch between the rather coarse model resolution (2.5° × 1.27°) and the much finer resolution of the satellite observations (∼0.1°). The data assimilated by the system correspond to the median observations inside the model grid-box, which inevitably loses information and reduces representativeness. Our approach to creating superobservations is likely to lead to an underestimation of the potential contribution of high-density products such as TROPOMI. Increasing the observation count and model resolution would help to better capture localized sources such as oil and gas production basins, which are typically a few hundred kilometers in size and composed of thousands of individual point sources that add up to large regional totals (Jacob et al., 2022). However, at the global scale this becomes very expensive computationally. Future satellite missions will provide even higher resolutions, making this issue even more critical. For example, ESA is developing the Copernicus Anthropogenic CO_2 Monitoring mission (CO2M), a constellation of three satellites with global coverage and a spatial resolution of $2 \times 2\,\mathrm{km}^2$ (Reuter et al., 2025), designed to monitor global atmospheric CO_2, CH_4 and nitrogen dioxide (NO_2), with the first satellite (CO2M-A) scheduled for launch in 2026.

Beyond spatial resolution, another limitation concerns the representation of observation errors. In our OSSEs, we used a diagonal error covariance matrix R including instrument and proxy model errors, but neglecting off-diagonal terms. In reality, correlations exist: in dense in-situ networks due to synoptic-scale transport linking observations of the same or different species, and in satellite data when retrievals share input information or algorithms (e.g., depending on CO_2).Accounting for such correlations in R could provide a more realistic estimate of the information content and avoid slight overestimation of the Degrees of Freedom for Signal (DOFS), as discussed by Pison (2018). DOFS represents the number of independent pieces of information that can be retrieved from the observations and are estimated as the trace of the averaging kernel matrix, (Kopacz et al., 2010).

Another potential source of bias is the representation of the vertical methane distribution, particularly across the tropopause. In our OSSE framework, this issue is implicitly removed because the pseudo-observations are generated using the same transport model. However, in real-world inversions, mismatches between modeled and observed total-column CH_4 may arise not only from surface flux errors but also from misrepresentation of the stratospheric–tropospheric gradient. Wang et al. (2017) compared several global transport models against FTS (Fourier transform spectrometry) and satellite data, separating stratospheric and tropospheric partial columns, and showed that biases of 4–12 ppb occur in both layers, partly linked to errors in vertical transport. Such biases can significantly influence the interpretation of satellite-derived fluxes, as they introduce systematic model–observation differences unrelated to surface emissions.

Overall, these aspects including the horizontal and vertical resolutions of the model, the representativeness of the assimilated observations, and the treatment of correlated errors jointly determine the actual information content that can be extracted from current and future satellite missions. Addressing these limitations will be essential to ensure that the increased precision and coverage of next-generation observing systems translate into more accurate and physically consistent methane flux estimates.

https://doi.org/10.5194/egusphere-2025-5923
Preprint. Discussion started: 23 December 2025

5.3 Challenges in sectoral flux optimization and error covariance design

In one of our experiments, 11 emission sectors are optimized independently. While this approach increases realism by accounting for sector-specific spatial and temporal patterns, it also introduces challenges because several of these sources overlap in the same regions, making difficult their separation (for instance, agriculture and waste, or biomass burning and wetlands). Our results show that for some sectors, like coal and waste, separating them improves the optimization (see Fig.10), but for others, such as biomass burning, their contribution is too small to constrain them well.

Consistent with the previous high-resolution study of Chen et al. (2022), our results suggest that some anthropogenic sources, such as coal and oil, can be very effectively separated in posterior estimates, even when multiple sectors are optimized simultaneously (e.g., in China, coal and oil posterior error correlations were found to be near zero; Chen et al. (2022)). This indicates that, although overlapping sectors make it difficult to constrain certain fluxes (e.g., waste or biomass burning), other emissions with unique spatial signatures remain robustly estimable.

Most global top-down inversions, typically optimize only a few aggregated fluxes (e.g., wetlands, fossil fuels, agriculture and waste, biomass burning, and other natural sources (Saunois et al., 2025)) or even only the net flux. The aggregation reduces computational cost and is often considered more robust, given the widely recognized limited ability of atmospheric observations to discriminate between overlapping sources, and because the inverse problem is inherently under-constrained (more sectors introduce more unknowns without increasing the number of observations). Therefore, while our finer sectoral optimization may provide additional detail, it should also be interpreted with caution in regions where observational constraints are weak and sectoral overlap is strong. This widely recognized disaggregated flux optimization represents a methodological advance over standard practice, offering finer sectoral detail albeit at the cost of increased complexity. By optimizing multiple sectors simultaneously, we attempt to capture sector-specific differences in the uncertainty reduction, although this inevitably increases the dimensionality of the problem and may amplify collinearities between flux components (Houweling et al., 2017).

This challenge of separating overlapping sources is further linked to the design of the error covariance matrix B, as the choice of spatial and temporal correlations in the prior strongly affects how information is distributed between sectors and regions. In our OSSE experiment, where sectors were optimized separately, we adopted a configuration with correlations defined by emission sector but uniform across the regions listed in Table 1 (Section 3.6). While still a simplification, this represents a step forward compared to many inversion systems that apply globally fixed or weakly structured correlations. As mentioned in Section 3.4, these examples illustrate the diversity of correlation structures used in global methane inversions, with a $\mathbf{B}$ matrix adapted to the heterogeneity of sectors and their underlying emission processes, and they highlight the trade-off between physical realism and numerical tractability when designing the prior error covariance matrix.

As a complementary perspective, isotopes and co-emitted tracers have been shown to help discriminate methane sources (Pison et al., 2009; Saunois et al., 2016; Basu et al., 2022; Thanwerdas et al., 2024). Integrating isotopic constraints with sector-specific error structures could improve source separability in future work. For example, δ^{13}C and δD measurements can provide additional information on the relative contributions of different regional and sectorial CH_4 sources.

https://doi.org/10.5194/egusphere-2025-5923
Preprint. Discussion started: 23 December 2025

Recent studies have demonstrated that $\delta^{13}C$ data can effectively distinguish between microbial and fossil CH_4 emissions at global and continental scales, but that this capability rapidly declines at smaller spatial scales due to the sparse and uneven distribution of isotopic measurements (Basu et al., 2022). Several limitations exist: overlapping isotopic signatures can reduce discriminative power at regional scales (Bergamaschi et al., 2015), atmospheric transport mixes signals and makes source separation difficult, and the network of isotopic observations is still much sparser than that of total CH_4.

Large and systematic uncertainties in $\delta^{13}C$ source signatures, together with the difficulty of defining realistic prior error covariances, still limit their applicability in inversion frameworks. These uncertainties are often non-Gaussian and stem from the limited representativeness of available isotopic datasets. Ensemble approaches and sensitivity tests using alternative $\delta^{13}C$ signature maps (Basu et al., 2022; Thanwerdas et al., 2024) provide practical means to assess robustness and partly overcome these limitations

In summary, while sectoral optimization and advanced error covariance structures increase realism, they also magnify the challenges of flux separability, highlighting the need for complementary information from isotopes, co-emitted tracers, and improved observing networks.

5.4 Methodological perspectives: beyond a unique 4D-Var solution

By design, 4D-Var provides a single deterministic solution, corresponding to the maximum a posteriori estimate of the fluxes considering a given configuration of components, and does not explicitly sample the full posterior distribution or explore highly non-linear model responses (Peters et al., 2005; Meirink et al., 2008). This limitation is particularly relevant when assessing the robustness of sector-specific flux estimates, where error correlations and prior assumptions play a major role.

To partially address this issue, we implemented a small Monte Carlo ensemble of 10 members by perturbing the prior flux fields. This allowed us to explore the sensitivity of the inversion results to prior assumptions and provided a first step toward evaluating robustness within the 4D-Var framework. Although the ensemble size was limited, it already highlighted the potential value of ensemble-based approaches for complementing variational inversions.

Future extensions could include larger ensembles or hybrid frameworks that combine the strengths of 4D-Var and ensemble methods. For example, Liu et al. (2017) demonstrated that an ensemble of 30 members can capture the influence of observational density on urban NOx emissions, suggesting that similar strategies could be applied to methane inversions at regional to global scales.

5.5 From regional constraints to national-scale applicability: opportunities and limitations

In our OSSEs, we adopted a regional framework (18 continental regions), consistent with international initiatives such as the Global Methane Budget (Saunois et al., 2025). While this approach facilitates comparability across studies and ensures methodological coherence, mitigation policies and reporting obligations are defined at the national scale under the United Nations Framework Convention on Climate Change (UNFCCC, 2014). Bridging the gap between regional inversions and national reporting therefore remains a central challenge.

https://doi.org/10.5194/egusphere-2025-5923
Preprint. Discussion started: 23 December 2025

As emphasized in several studies (Dlugokencky et al., 2011; Saunois et al., 2025; Jacob et al., 2022), observational coverage remains highly uneven, with some regions much better constrained than others. In particular, tropical areas and parts of the Southern Hemisphere continue to suffer from sparse observational density, which limits the ability of top-down inversions to provide robust flux estimates at national scales. Our results confirm these limitations: GN+S and TROPOMI could approach this scale in regions with good coverage, but in the tropics and Southern Hemisphere the coverage remains insufficient.

In addition, the relatively coarse resolution of our transport model (2.5° in longitude × 1.27° in latitude) inherently limits the applicability of our results at the national scale. At this resolution, small or narrow countries—such as those in Europe or the Middle East—may fall within a single grid cell, making it difficult to represent fine-scale processes and local emission patterns. As a result, urban areas or specific industrial regions cannot be explicitly resolved, which adds further uncertainty when comparing inversion results with national emission inventories.

Overall, while regional OSSEs provide valuable insights into the potential of observing systems, advancing towards robust national-scale assessments will require both enhanced observational density and higher-resolution transport modeling capable of resolving sub-national emission patterns. Monitoring of national GHG emissions could be tested for France with a limited increase of the ICOS observing network, the use of regional models such a CHIMERE, the operationalization of inversions, and a reasonable investment considering the strategical objective to produce robust budgets at national scales in the context of Paris agreement and French Nationally Determined Contributions (NDCs).

5.6 Satellite Observing Systems: Current Capabilities and Future Perspective

5.6.1 Satellite products and complementarity

As shown in Section 4.1, we found that in our study the performance of TROPOMI was overall comparable to GOSAT, despite TROPOMI having higher spatial and temporal coverage. Interestingly, our results also indicate that more numerous observations with larger random errors (TROPOMI) are not always more effective than fewer but more precise ones (GOSAT). This is consistent with Qu et al. (2021), who reported that at the global 2° × 2.5° resolution, GOSAT inversions achieved higher information content (DOFS = 232) compared to TROPOMI (DOFS = 151), even though TROPOMI provides 100 times more observations. They attribute this to spatial error correlations and the uneven distribution of TROPOMI data, which reduces its effective constraint at coarse resolutions. As also noted in their study, the full potential of TROPOMI is better exploited at finer spatial resolution in regional inversions. In our OSSE framework, we used pseudo-observations without including retrieval biases; therefore, our results reflect the maximum potential of the satellite products in idealized conditions.

Another key finding from Qu et al. (2021) is that combining GOSAT and TROPOMI yields stronger constraints than either dataset alone. This suggests that complementarity between different satellite products may provide a way to balance precision, coverage, and bias correction in future inversion frameworks. Beyond satellite-only configurations, we also tested the added value of integrating surface and satellite observations. As discussed in Section 4.2, our results show that joint assimilations provide stronger constraints than using either system separately, in agreement with previous work (Lu et al., 2021; Liang et al., 2023). These studies demonstrated that while GOSAT delivers strong global constraints, in situ observations are crucial

https://doi.org/10.5194/egusphere-2025-5923
Preprint. Discussion started: 23 December 2025

in northern midlatitudes and in reducing error correlations between methane emissions. The combination is therefore more powerful than either dataset alone.

Other satellite products are also emerging that could enhance future methane inversion studies and could be incorporated into our framework. For example, Tsuruta et al. (2025) evaluated a GOSAT-based retrieval of the lower-troposphere partial column ($pXCH_4$_LT) and showed that it can substantially reduce uncertainties in tropical regions and in areas with sparse surface observations. They also found that surface measurements remain most effective in North America and Europe, while GOSAT provides stronger constraints in Asia and the tropics—consistent with the regional patterns we identified in our OSSEs. Likewise, the ESA METHANE+ project has developed a joint methane retrieval using Sentinel-5P and IASI, exploiting their complementary vertical sensitivities to better capture methane variability in the lower troposphere (Buchwitz et al., 2023). These emerging datasets offer promising opportunities for future applications of our approach, as they could be integrated directly into the same OSSE and inversion framework to assess their added value and to explore how improved vertical sensitivity or precision influences posterior flux estimates.

5.6.2 Perspectives with upcoming satellite missions

Looking ahead, several recently launched and upcoming missions promise to strengthen the global methane observing system. GOSAT-GW (June 2025; Tanimoto et al. 2025) continues the GOSAT legacy with a 3-day repeat cycle and expanded 10 × 10 km^2 spatial coverage, delivering consistent and accurate column measurements. MERLIN (2029; Ehret et al. 2017; Bousquet et al. 2018), an active Integrated path differential absorption (IPDA) lidar mission, will provide high-accuracy methane observations globally, including high latitudes, winter months and partially cloudy regions, with minimal systematic errors (<2 ppb) and reduced sensitivity to thin cirrus or aerosol layers; however, its 28-day repeat cycle limits detection of short-lived events. IASI-NG (August 2025; Crevoisier et al. 2014) ensures continuity of the IASI mission while doubling key performance capabilities, offering upper-troposphere–lower-stratosphere profiles that complement column observations from instruments as TROPOMI (Schneider et al., 2022) and Sentinel5-A (European Space Agency (ESA), 2025). Collectively, these advances promise significant improvements in coverage, precision, and robustness for methane flux estimation. Nevertheless, persistent cloud cover and other observational limitations will leave some regions effectively "blind," highlighting the continued need for complementary in-situ measurements and dedicated field campaigns (e.g., AirCore, spectrometers, and aircraft profiles) to improve vertical characterization and achieve more balanced global constraints.

6 Conclusions

This study evaluate the potential of current observing systems to monitor methane emissions at the regional to the global scales through OSSEs. By optimizing either total net fluxes or 11 sector-specific fluxes across 18 regions, we quantified how well different observing systems constrain emissions and reduce their uncertainties. Our results show that, optimizing net fluxes, high-flux regions, particularly in the Northern Hemisphere, are effectively constrained by in-situ and satellite systems, reaching uncertainty reduction values of up to 50% in in-situ–based inversions over the United States, Canada, Europe, and China, and

https://doi.org/10.5194/egusphere-2025-5923
Preprint. Discussion started: 23 December 2025

between 10–50% with satellite observations over the same regions. In contrast, regions in the Southern Hemisphere remain blind spots with much weaker observational constraints. Combining satellite and surface observations further improves performance. In particular, the GOSAT-NIES+Surface configuration showed the strongest results, achieving uncertainty reductions above 20% in half of the regions and as high as 50% in 11 out of 18 regions, demonstrating the strong complementarity of different observing systems, especially in areas with sparse in-situ coverage.

At the sectoral level, our analysis highlights that high-emission sectors, such as agriculture in South Asia, coal in China, and oil and gas in the Middle East, can be effectively constrained by combinations of surface and satellite observations. In contrast, more widespread or relatively low-emission sectors, such as biomass burning and waste, remain poorly constrained. These results underline both the potential and the limits of sectoral flux optimization in global inversions.

Looking forward, recently launched and upcoming satellite missions, together with expanded in-situ networks and targeted field campaigns, will strengthen methane monitoring capabilities by improving spatial coverage, vertical sensitivity, and overall robustness of flux estimates. While persistent gaps will remain in regions with extensive cloud cover or limited measurements, integrating multiple observing systems will be essential to achieving more accurate and spatially consistent constraints, and to better representing their random and systematic uncertainties. Collectively, these advances promise progress in delivering the precision needed for national-scale methane emission reporting and for guiding effective mitigation strategies.

Data availability. Observational methane data from the NOAA network were obtained from the ObsPack-CH_4 GLOBALVIEWplus v4.0 (2021-10-14) and ObsPack-CH_4 NRTv3.0 (2021-05-18) products, available at https://gml.noaa.gov/ccgg/obspack/ (last access: 1 February 2022). ICOS Near Real-Time (Level 1) atmospheric CO_2, CO, and CH_4 mole-fraction data are available at https://doi.org/10.18160/ATM_NRT_CO2_CH4 (last access: 1 April 2022). CSIRO greenhouse gas observations were retrieved from the WMO World Data Centre for Greenhouse Gases (WDCGG), available at https://gaw.kishou.go.jp/ (last access: 1 April 2022). Anthropogenic methane emissions from the EDGAR v6.0 and EDGAR v7.0 inventories can be downloaded from https://edgar.jrc.ec.europa.eu/dataset_ghg60 (last access: 1 October 2023) and https://edgar.jrc.ec.europa.eu/dataset_ghg70 (last access: 1 October 2023), respectively. GOSAT-NIES SWIR V02.96 level 2 data are available from the GOSAT Data Archive Service at https://data2.gosat.nies.go.jp (last access: 1 July 2023). GOSAT Proxy XCH_4 v9.0 data can be downloaded from the CEDA archive at https://dx.doi.org/10.5285/18ef8247f52a4cb6a14013f8235cc1eb (last access: 1 July 2023). IASI-METOP-A atmospheric composition data are available from AERIS at https://iasi.aeris-data.fr (last access: 1 April 2021). TROPOMI-WFMD v1.8 XCH_4 data are available at https://www.iup.uni-bremen.de/carbon_ghg/products/tropomi_wfmd/ (last access: 24 October 2023).

Author contributions. NM, MS, and AB designed the study. NM performed all OSSE experiments. MS and AB contributed to the scientific discussion and provided systematic technical and scientific guidance throughout the work. JT and AM contributed to code development and provided technical support. AM and IP contributed additional scientific expertise and critical feedback. All authors contributed to the revision and improvement of the manuscript.

https://doi.org/10.5194/egusphere-2025-5923
Preprint. Discussion started: 23 December 2025

Competing interests. The contact author has declared that neither they nor their co-authors have any competing interests.

Acknowledgements. Computations were carried out using the LSCE computing resources, maintained by Julien Bruna and the LSCE IT team. Additionally, this study was provided with HPC and storage resources by GENCI at TGCC thanks to the grant 2025-2201 on the supercomputer Joliot Curie's V100 partition. The authors used OpenAI's ChatGPT to assist with language editing. All content was verified and approved by the authors.

Financial support. The publication of this article was supported by the Agence Nationale de la Recherche (ANR) through the project Advanced Methane Budget through Multi-constraints and Multi-data streams Modelling (grant no. c). Author acknowledges the support from ANID through the PhD fellowship "ANID BECAS/DOCTORADO EN EL EXTRANJERO (Becas Chile) 72220111 and the support from CNES through a doctoral fellowship 5100020500.

https://doi.org/10.5194/egusphere-2025-5923
Preprint. Discussion started: 23 December 2025

Appendix A: Observational inputs

This section provides additional details on the observational datasets and their preprocessing steps. Figures include examples of averaging kernels and vertical sensitivity, mean observational errors, and the number of super-observations aggregated by region and observing system in 2019. These diagnostics complement the description in the Data and Methods section by illustrating the properties of the inputs assimilated in the inversion framework.

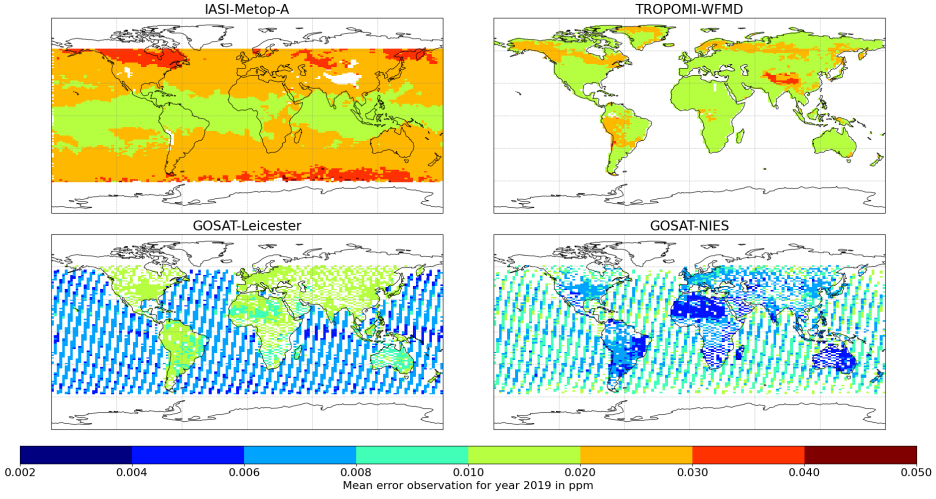

Figure A1. Average error of the 2019 super-observations, computed across the four satellite products incorporated in this study.

https://doi.org/10.5194/egusphere-2025-5923
Preprint. Discussion started: 23 December 2025

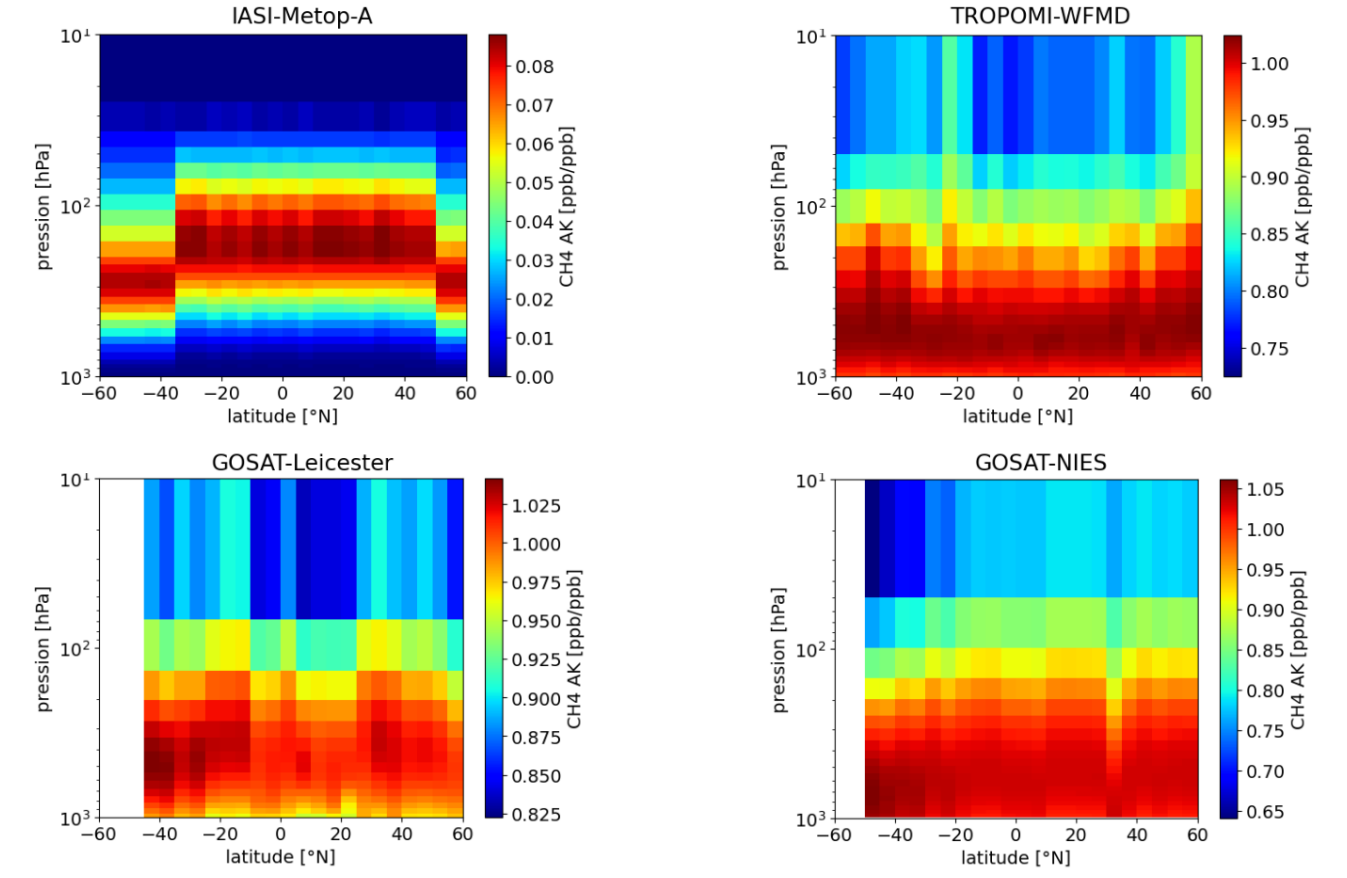

Figure A2. Averaging kernel and vertical pressure obtained from median observations by latitude in July 2019.

https://doi.org/10.5194/egusphere-2025-5923
Preprint. Discussion started: 23 December 2025

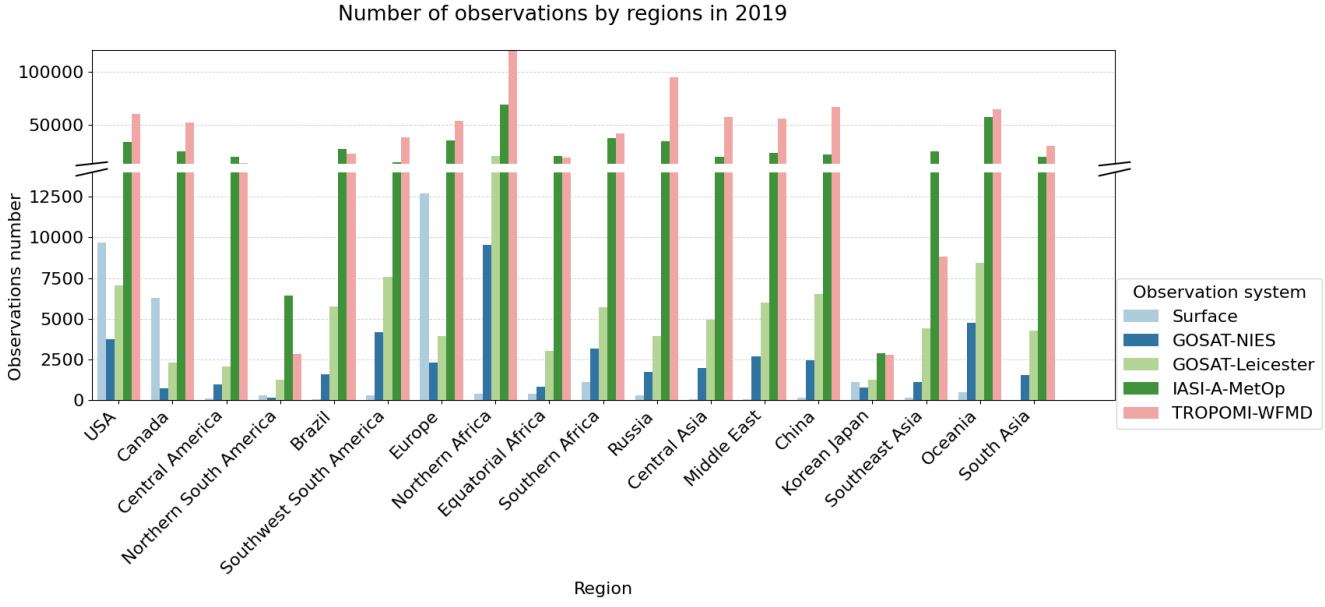

Figure A3. Super-observations count by region and observing system in 2019.

https://doi.org/10.5194/egusphere-2025-5923
Preprint. Discussion started: 23 December 2025

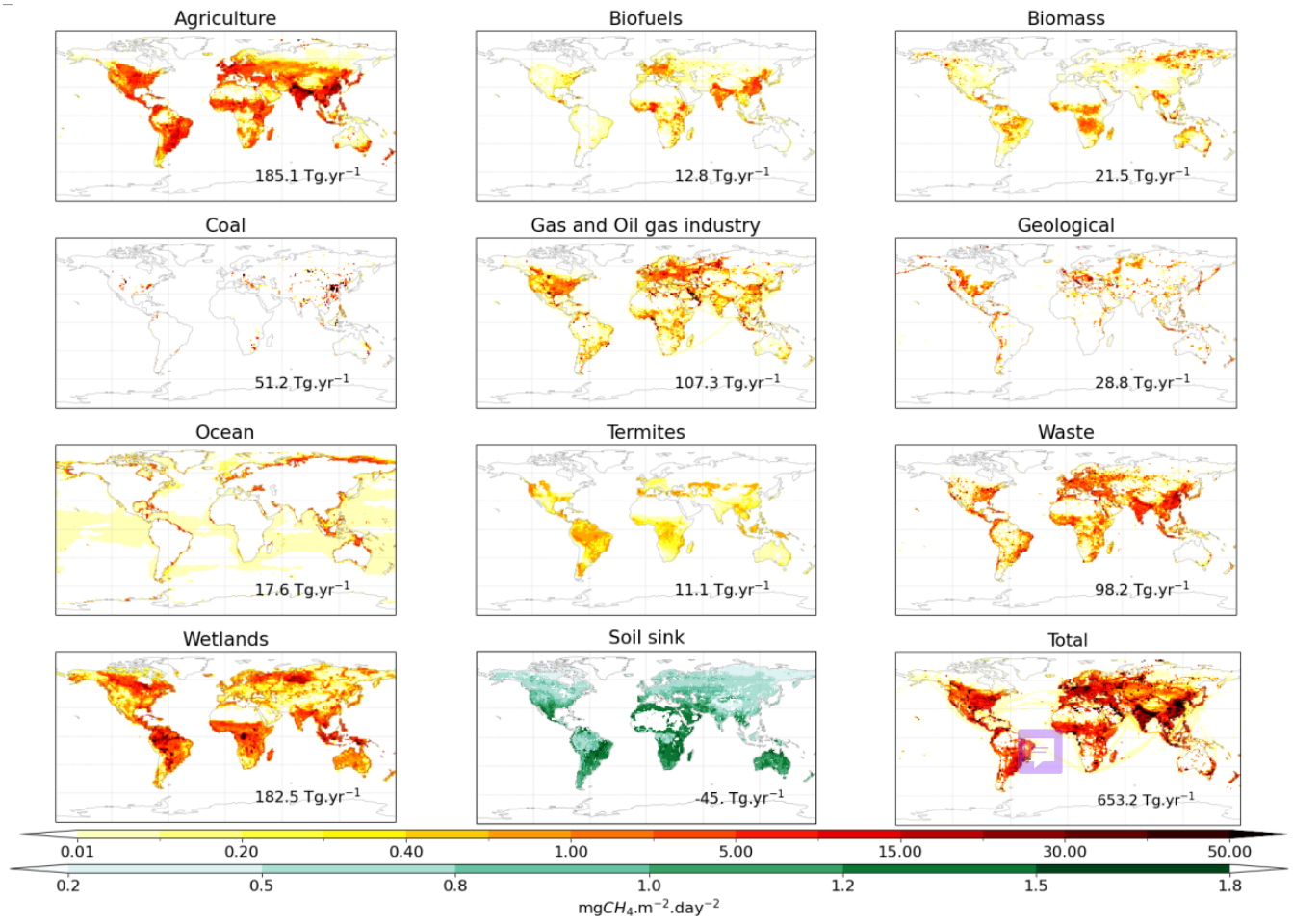

Figure A4. Methane sources and sinks from eleven source categories for the 2019 monthly mean (mg CH_4 m^{-2} d^{-1}). Please note the different color maps for sources (white to red) and sinks (white to green), as well as different scales.

925

https://doi.org/10.5194/egusphere-2025-5923
Preprint. Discussion started: 23 December 2025

Table A1. Monitoring stations used in this study (Part 1), with station name, network, latitude, longitude, altitude, and instrumental error + model error (IE+ME)

Station	Network	Longitude	Latitude	Altitude	IE+ME	Station	Network	Lon	Lat	Alt	IE+ME
abt	eccc	-122.3	49.0	93	42.6	dsi	noaa	116.7	20.7	8	38.0
alt	noaa	-62.5	82.5	197	9.2	egb	eccc	-79.8	44.2	276	36.0
ams	icos-atc/lsce	77.5	-37.8	75	2.7	eic	noaa	-109.4	-27.2	69	4.3
amt	noaa	-68.7	45.0	160	20.4	ena	lbnl-arm	-28.0	39.1	30	15.6
amv	icos-atc/um5	-5.1	33.4	2051	16.3	ers	icos-atc/lsce	9.4	43.0	573	18.5
amy	kma	126.3	36.5	69	74.4	esp	eccc	-126.5	49.4	47	11.4
asc	noaa	-14.4	-8.0	90	5.9	est	eccc	-110.2	51.7	757	65.6
ask	noaa	5.6	23.3	2715	9.0	etl	eccc	-105.0	54.4	598	20.6
azr	noaa	-27.4	38.8	24	18.2	fkl	icos-atc/ecpl	25.7	35.3	265	18.1
azv	nies	73.0	54.7	160	59.1	fne	eccc	-122.6	58.8	376	21.8
bck	eccc	-115.9	62.8	220	14.7	fsd	eccc	-81.6	49.9	250	13.3
bhd	noaa	174.9	-41.4	95	6.1	gat	icos-atc/hpb	11.4	53.1	411	26.8
bis	icos-atc/lsce	-1.2	44.4	120	26.2	gci01	psu	-92.3	32.5	165	39.6
bkt	noaa	100.3	-0.2	875	27.9	gci02	psu	-89.9	33.8	205	37.5
blk	eccc	-96.0	64.3	61	9.9	gmi	noaa	144.7	13.4	5	17.5
bmw	noaa	-64.9	32.3	51	20.1	gpa	csiro	131.0	-12.2	37	26.1
bra	eccc	-104.7	50.2	630	28.9	guy	icos-atc/ecofog	-52.9	5.3	97	15.2
brw	noaa	-156.6	71.3	26	24.4	hba	noaa	-26.2	-75.6	35	4.1
brz	nies	84.3	56.1	248	37.2	hle	icos-atc	79.0	32.8	4517	32.9
bsd	univbris	-1.1	54.4	628	22.5	hnp	eccc	-79.4	43.6	97	46.2
cba	noaa	-162.7	55.2	57	15.4	hpb	icos-atc/hpb	11.0	47.8	1049	33.7
cby	eccc	-105.1	69.1	47	11.2	htm	icos-atc/cec	13.4	56.1	265	24.1
cfa	csiro	147.1	-19.3	5	11.1	hun	noaa	16.6	47.0	354	31.0
cgo	noaa	144.7	-40.7	147	7.9	ice	noaa	-20.3	63.4	122	10.8
chc	icos-atc/lfa	-68.1	-16.4	5255	20.5	inu	eccc	-133.5	68.3	123	15.9
chl	eccc	-93.8	58.7	89	15.2	inx	noaa	-86.0	39.8	403	31.0
chr	noaa	-157.2	1.7	5	8.7	inx01	psu	-86.4	39.6	377	34.4
cib	noaa	-4.9	41.8	850	23.5	inx02	psu	-86.0	39.8	403	34.4
cmn	icos-atc/cnr-isac	10.7	44.2	2173	20.2	inx03	psu	-86.2	39.8	280	39.3
cps	eccc	-75.0	49.8	431	13.6	inx04	psu	-86.1	39.6	309	36.4
cpt	saws	18.5	-34.4	260	12.1	inx07	psu	-86.3	39.8	299	43.8
cra	icos-atc/la	0.4	43.1	660	20.5	inx08	psu	-86.0	40.0	286	35.2
crv	noaa	-147.6	65.0	643	14.8	inx09	psu	-85.7	39.9	407	34.1
crz	noaa	51.8	-46.4	202	2.6	inx10	psu	-86.1	39.7	263	44.5
cvo	ceda/mpi-bgc	-24.9	16.9	40	12.5	inx11	psu	-86.2	39.8	344	35.4
cya	csiro	110.5	-66.3	55	9.1	inx13	psu	-85.9	39.7	335	35.2
dem	nies	70.9	59.8	126	51.5	inx14	psu	-86.7	40.0	340	34.3
drp	noaa	-63.8	-59.0	10	3.2	ipr	icos-atc/jrc	8.6	45.8	310	64.2

https://doi.org/10.5194/egusphere-2025-5923
Preprint. Discussion started: 23 December 2025

Table A2. Monitoring stations used in this study (Part 2), with station name, network, latitude, longitude, altitude, and instrumental error + model error.

Station	Network	Lon	Lat	Alt	IE+ME	Station	Network	Lon	Lat	Alt	IE+ME
izo	aemet	-16.5	28.3	2400	14.0	rpb	noaa	-59.4	13.2	20	11.2
jfj	icos-atc/hfsjg	8.0	46.5	3582	20.1	run	icos-atc/lsce	55.4	-21.1	2160	6.4
jgs	kma	126.2	33.3	77	48.9	rvrb	noaa	-46.5	23.0	15	8.5
key	noaa	-80.2	25.7	6	46.4	ryo	jma	141.8	39.0	280	16.9
kit	icos-atc/hpb	8.4	49.1	310	37.4	sac	icos-atc/cea	2.1	48.7	260	36.8
kre	icos-atc/cas	15.1	49.6	784	24.6	sct	noaa/srnl	-81.8	33.4	420	35.9
krs	nies	82.4	58.2	143	41.8	sey	noaa	55.5	-4.7	7	17.9
kum	noaa	-155.0	19.7	5	13.6	sgp	lbnl-arm	-97.5	36.6	332	68.2
lef	noaa	-90.3	45.9	868	24.9	shm	noaa	174.1	52.7	28	11.0
lew	noaa	-76.9	40.9	256	43.0	smo	noaa	-170.6	-14.2	54	7.9
lin	icos-atc/hpb	14.1	52.2	171	30.3	smr	icos-atc/inar	24.3	61.8	306	20.1
llb	eccc	-112.5	55.0	590	52.4	spo	csiro	-24.8	-90.0	2829	5.8
lln	noaa	120.9	23.5	2867	24.6	ste	icos-atc/hpb	8.5	53.0	281	43.9
lmp	noaa	12.6	35.5	52	14.7	str	noaa	-122.5	37.8	486	31.0
lto	icos-atc/lsce	-5.0	6.2	205	14.6	sum	noaa	-38.4	72.6	3215	9.7
lut	icos-atc/rug	6.4	53.4	61	80.3	svb	icos-atc/slu	19.8	64.3	419	16.6
maa	csiro	62.9	-67.6	42	9.1	syo	tu	39.6	-69.0	22	2.7
mbo	noaa	-121.6	43.7	2717	16.0	tac	univbris	1.1	52.5	241	31.8
mex	noaa	-97.3	19.0	4469	14.0	tap	noaa	126.1	36.7	21	51.5
mhd	icos-atc/nui	-9.9	53.3	29	25.0	tik	fmi/mgo	128.9	71.6	29	21.9
mid	noaa	-177.4	28.2	15	15.7	toh	icos-atc/hpb	10.5	51.8	948	22.0
mlo	noaa	-155.6	19.5	3433	13.5	tpd	eccc	-80.6	42.6	266	39.8
mnm	jma	154.0	24.3	27	16.9	trn	icos-atc/lsce	2.1	48.0	311	28.0
mqa	csiro	159.0	-54.5	13	9.4	uld	kma	130.9	37.5	231	28.3
mrc	psu	-76.4	41.5	652	35.7	ush	noaa	-68.3	-54.8	32	3.8
msh	noaa	-70.5	41.7	78	28.0	uta	noaa	-113.7	39.9	1332	28.1
mwo	noaa	-118.1	34.2	1774	36.2	uto	icos-atc/fmi	21.4	59.8	65	21.6
nat	noaa	-35.2	-5.8	87	20.4	uum	noaa	111.1	44.5	1012	22.6
nmb	noaa	15.0	-23.6	461	8.7	vgn	nies	62.3	54.5	277	31.6
nor	icos-atc/lund-cec	17.5	60.1	146	18.7	wbi	noaa	-91.4	41.7	621	34.5
noy	nies	75.8	63.4	151	66.3	wgc	noaa/lbnl	-121.5	38.3	374	59.1
nwr	noaa	-105.6	40.1	3526	22.2	wis	noaa	35.1	30.0	156	28.1
ohp	icos-atc/osu	5.7	43.9	750	19.3	wkt	noaa	-97.3	31.3	373	56.8
oli	lbnl-arm	-149.9	70.5	2	48.4	wlg	noaa	100.9	36.3	3815	18.8
ope	icos-atc/andra	5.5	48.6	510	29.2	wsa	eccc	-60.0	43.9	8	15.1
oxk	noaa	11.8	50.0	1185	22.7	wsd	psu	-98.6	44.1	652	34.1
pal	icos-atc/fmi	24.1	68.0	576	19.2	yon	jma	123.0	24.5	50	29.9
pdm	icos-atc	0.1	42.9	2904	24.0	zep	icos-atc/nilu	11.9	78.9	488	9.9
psa	noaa	-64.1	-64.8	15	2.4						
puy	icos-atc/lsce	3.0	45.8	1475	20.9						
rgl	univbris	-2.5	52.0	294	37.4						

https://doi.org/10.5194/egusphere-2025-5923
Preprint. Discussion started: 23 December 2025

Appendix B: Complementary uncertainty and performance analyses

This section presents additional figures supporting the main analysis of uncertainty reduction and system performance. We report pairwise relationships among key variables, regional and national performance metrics, and spatial patterns of posterior uncertainty reduction. These results provide further insight into the heterogeneity of system performance across regions, sectors, and spatial scales, complementing the main findings discussed in the Results section.

https://doi.org/10.5194/egusphere-2025-5923
Preprint. Discussion started: 23 December 2025

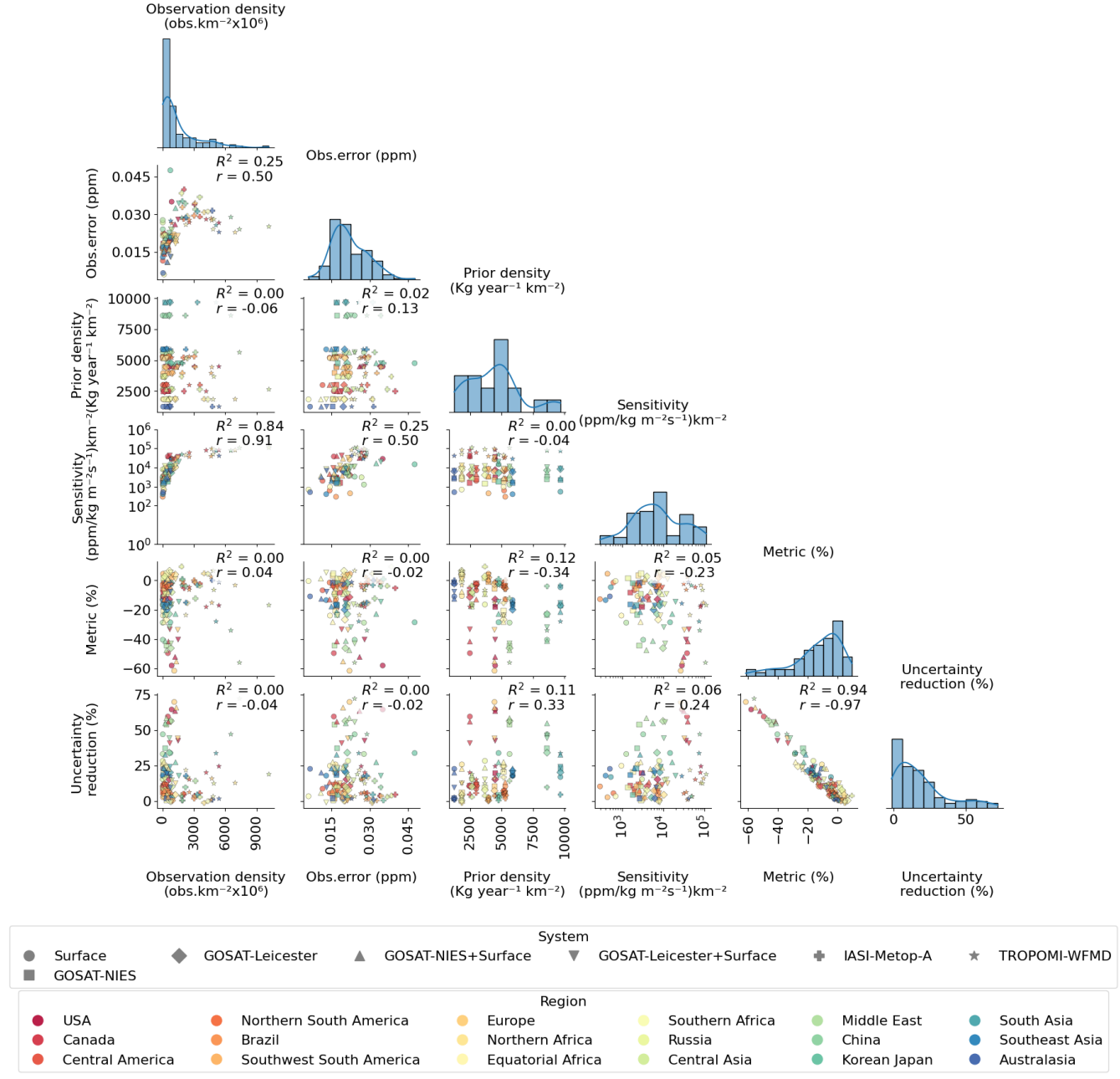

Figure B1. Scatterplot matrix (lower triangular) showing the relationships among key variables for the seven observing systems across 18 regions: observation density, observation error, prior flux density, performance metric, and uncertainty reduction. Each panel illustrates pairwise correlations between variables.

https://doi.org/10.5194/egusphere-2025-5923
Preprint. Discussion started: 23 December 2025

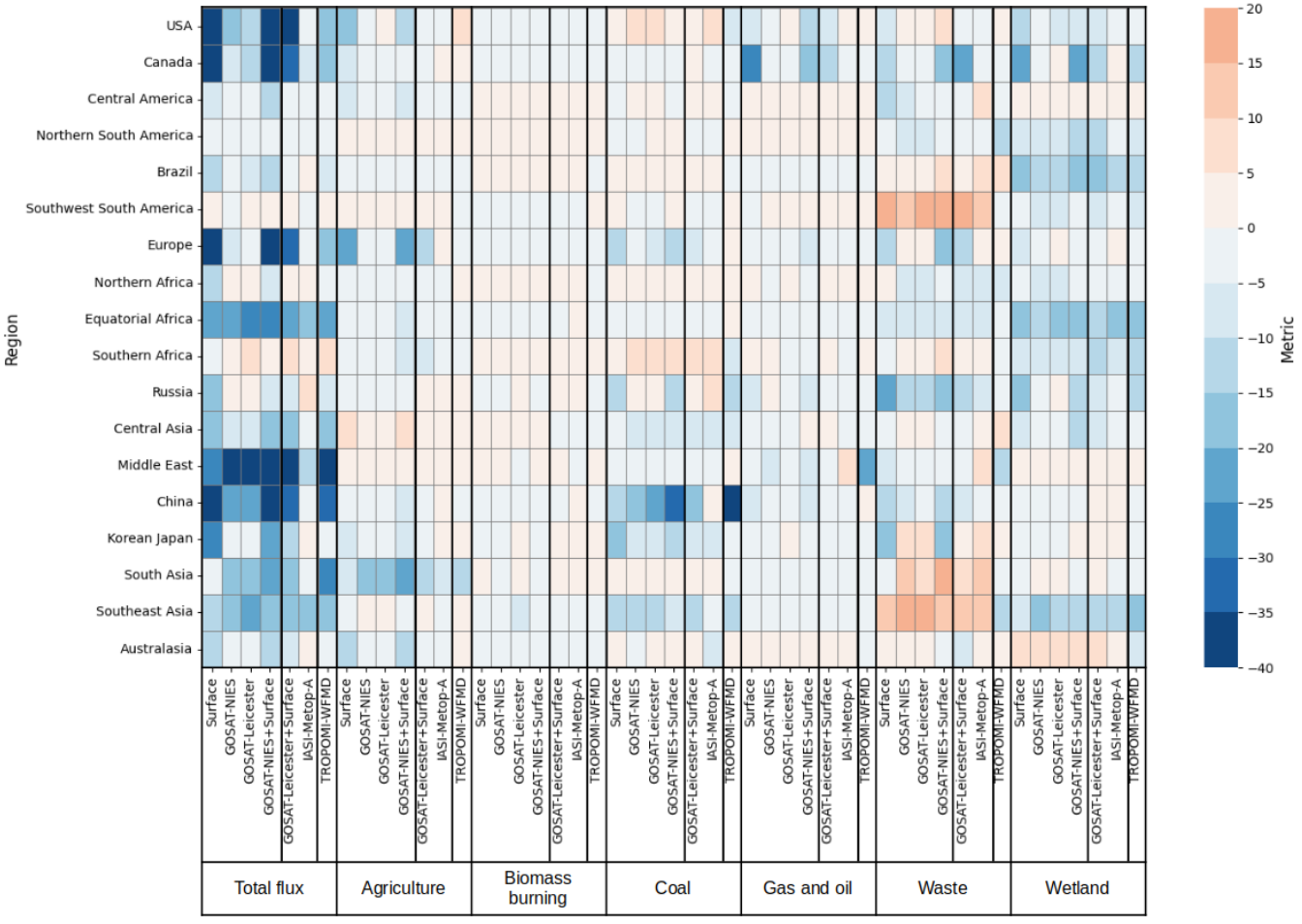

Figure B2. UR for optimization experiments targeting total flux and individual sectors. Results are shown for seven observing systems and evaluated across 18 regions trough OSSEs..

https://doi.org/10.5194/egusphere-2025-5923
Preprint. Discussion started: 23 December 2025

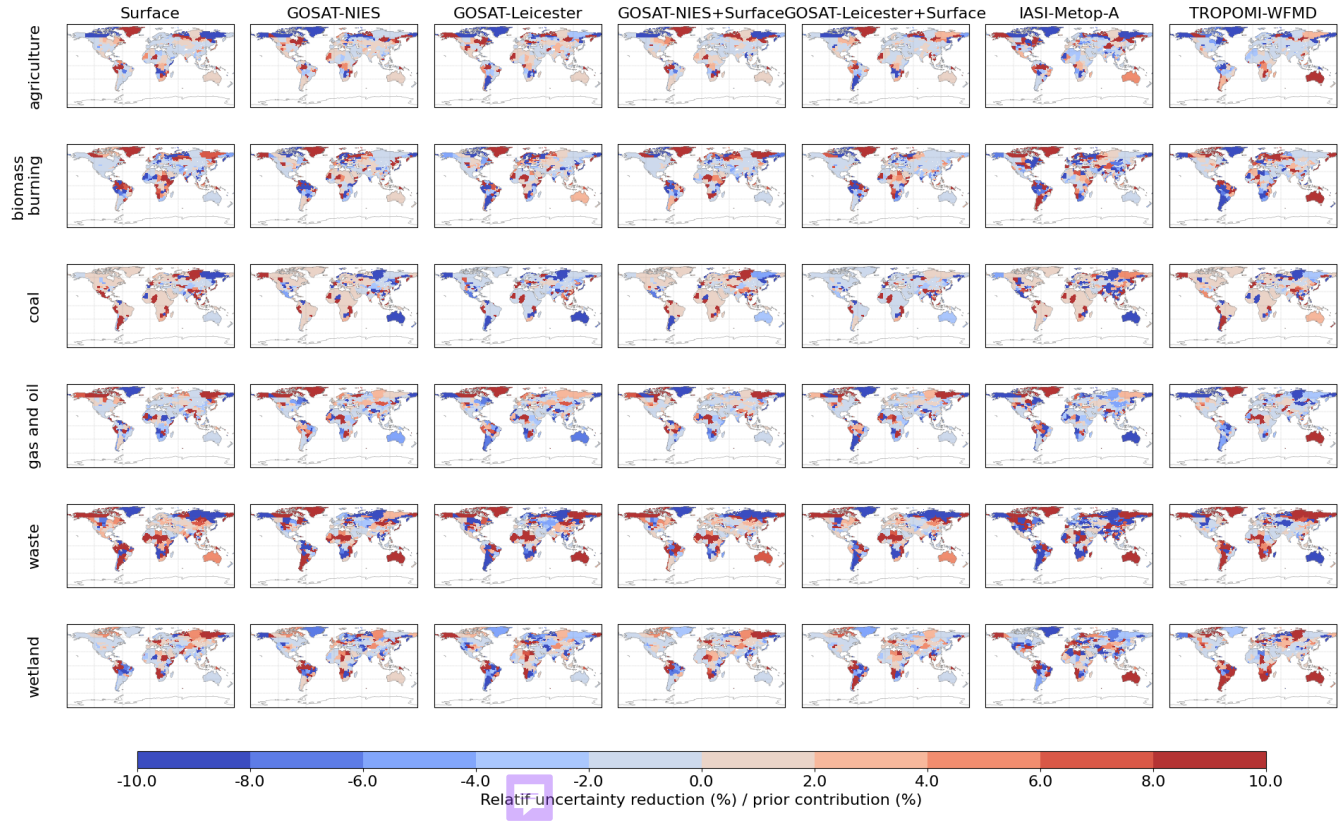

Figure B3. Relative Sectoral Uncertainty Reduction (RSUR, %) at country scale for six methane emission sectors across seven observing system configurations

https://doi.org/10.5194/egusphere-2025-5923
Preprint. Discussion started: 23 December 2025

Figure B4. Reduction of uncertainty in the distribution of sectoral fluxes. Each point represents one sector within a given region. The x-axis indicates the sectoral contribution to total prior emissions, and the y-axis shows its contribution to total uncertainty reduction. Points lying close to the red line denote sectors whose uncertainty reduction is approximately proportional to their emission share, corresponding to near-zero RSUR values.

https://doi.org/10.5194/egusphere-2025-5923
Preprint. Discussion started: 23 December 2025

References

AERIS Atmospheric Data Centre: IASI Atmospheric Composition Data Products, https://iasi.aeris-data.fr, 2021.

Andrews, A., Kofler, J., Trudeau, M., Williams, J., Neff, D., Masarie, K., Chao, D., Kitzis, D., Novelli, P., Zhao, C., et al.: CO 2, CO, and CH 4 measurements from tall towers in the NOAA Earth System Research Laboratory's Global Greenhouse Gas Reference Network: Instrumentation, uncertainty analysis, and recommendations for future high-accuracy greenhouse gas monitoring efforts, Atmospheric Measurement Techniques, 7, 647–687, 2014.

Balasus, N., Jacob, D. J., Lorente, A., Maasakkers, J. D., Parker, R. J., Boesch, H., Chen, Z., Kelp, M. M., Nesser, H., and Varon, D. J.: A blended TROPOMI+ GOSAT satellite data product for atmospheric methane using machine learning to correct retrieval biases, Atmospheric Measurement Techniques, 16, 3787–3807, 2023.

Basu, S., Lan, X., Dlugokencky, E., Michel, S., Schwietzke, S., Miller, J. B., Bruhwiler, L., Oh, Y., Tans, P. P., Apadula, F., et al.: Estimating emissions of methane consistent with atmospheric measurements of methane and δ 13 C of methane, Atmospheric Chemistry and Physics, 22, 15 351–15 377, 2022.

Beer, R., Glavich, T. A., and Rider, D. M.: Tropospheric emission spectrometer for the Earth Observing System's Aura satellite, Applied optics, 40, 2356–2367, 2001.

Berchet, A., Sollum, E., Thompson, R. L., Pison, I., Thanwerdas, J., Broquet, G., Chevallier, F., Aalto, T., Berchet, A., and Bergamaschi, P., e. a.: The Community Inversion Framework v1. 0: A unified system for atmospheric inversion studies, Geoscientific Model Development, 14, 5331–5354, 2021.

Bergamaschi, P., Corazza, M., Karstens, U., Athanassiadou, M., Thompson, R. L., Pison, I., Manning, A. J., Bousquet, P., Segers, A., Vermeulen, A., et al.: Top-down estimates of European CH 4 and N 2 O emissions based on four different inverse models, Atmospheric Chemistry and Physics, 15, 715–736, 2015.

Bousquet, P., Pierangelo, C., Bacour, C., Marshall, J., Peylin, P., Ayar, P. V., Ehret, G., Bréon, F.-M., Chevallier, F., Crevoisier, C., et al.: Error budget of the MEthane Remote LIdar missioN and its impact on the uncertainties of the global methane budget, Journal of Geophysical Research: Atmospheres, 123, 11–766, 2018.

Brasseur, G. P. and Jacob, D. J.: Modeling of atmospheric chemistry, Cambridge University Press, 2017.

Buchwitz, M., a. O., Vanselow, S., Houweling, S., Van Peet, J., Siddans, R., Kerridge, B., , Ventress, L., Knappett, D., Crevoisier, C., Meilhac, N., Borsdorf, T., and Lorente, A. Aben, I.: Final report ESA project METHANE+ led by SRON, 2023.

Chen, Z., Jacob, D., Nesser, H., Sulprizio, M., Lorente, A., Varon, D., Lu, X., Shen, L., Qu, Z., Penn, E., et al.: Methane emissions from China: a high-resolution inversion of TROPOMI satellite observations, Atmospheric Chemistry and Physics Discussions, 2022, 1–31, 2022.

Clerbaux, C., Hadji-Lazaro, J., Turquety, S., George, M., Coheur, P.-F., Hurtmans, D., Wespes, C., Herbin, H., Blumstein, D., Tourniers, B., and Phulpin, T.: The IASI/MetOp1 Mission: First observations and highlights of its potential contribution to GMES2, Space Research Today, 168, 19–24, https://doi.org/https://doi.org/10.1016/S0045-8732(07)80046-5, 2007.

Clerbaux, C., Boynard, A., Clarisse, L., George, M., Hadji-Lazaro, J., and Herbin, H., a. a.: Monitoring of atmospheric composition using the thermal infrared IASI/MetOp sounder, Atmospheric Chemistry and Physics, 9, 6041–6054, https://doi.org/10.5194/acp-9-6041-2009, 2009.

https://doi.org/10.5194/egusphere-2025-5923
Preprint. Discussion started: 23 December 2025

Cressot, C., Chevallier, F., Bousquet, P., Crevoisier, C., Dlugokencky, E., Fortems-Cheiney, A., Frankenberg, C., Parker, R., Pison, I., Scheepmaker, R., et al.: On the consistency between global and regional methane emissions inferred from SCIAMACHY, TANSO-FTS, IASI and surface measurements, Atmospheric Chemistry and Physics, 14, 577–592, 2014.

Cressot, C., Pison, I., Rayner, P. J., Bousquet, P., Fortems-Cheiney, A., and Chevallier, F.: Can we detect regional methane anomalies? A comparison between three observing systems, Atmospheric Chemistry and Physics, 16, 9089–9108, 2016.

Crevoisier, C., Nobileau, D., Fiore, A., Armante, R., Chédin, A., and Scott, N.: Tropospheric methane in the tropics–first year from IASI hyperspectral infrared observations, Atmospheric Chemistry and Physics, 9, 6337–6350, 2009.

Crevoisier, C., Clerbaux, C., Guidard, V., Phulpin, T., Armante, R., Barret, B., Camy-Peyret, C., Chaboureau, J.-P., Coheur, P.-F., Crépeau, L., Dufour, G., Labonnote, L., Lavanant, L., Hadji-Lazaro, J., Herbin, H., Jacquinet-Husson, N., Payan, S., Péquignot, E., Pierangelo, C., Sellitto, P., and Stubenrauch, C.: Towards IASI-New Generation (IASI-NG): impact of improved spectral resolution and radiometric noise on the retrieval of thermodynamic, chemistry and climate variables, Atmospheric Measurement Techniques, 7, 4367–4385, https://doi.org/10.5194/amt-7-4367-2014, 2014.

Crippa, M., Guizzardi, D., Solazzo, E., Muntean, M., Schaaf, E., Monforti-Ferrario, F., Banja, M., Olivier, J. G. J., Grassi, G., Rossi, S., and Vignati, E.: GHG emissions of all world countries – 2021 Report, Tech. Rep. JRC126363, Publications Office of the European Union, Luxembourg, ISBN 978-92-76-41547-3, https://doi.org/10.2760/173513, 2021.

Dlugokencky, E., Crotwell, A., Mund, J., Crotwell, M., and Thoning, K.: Atmospheric Methane Dry Air Mole Fractions from the NOAA GML Carbon Cycle Cooperative Global Air Sampling Network, Version 2020-07, https://doi.org/10.15138/VNCZM766, 2020.

Dlugokencky, E. J., Nisbet, E. G., Fisher, R., and Lowry, D.: Global atmospheric methane: budget, changes and dangers, Philosophical Transactions of the Royal Society A: Mathematical, Physical and Engineering Sciences, 369, 2058–2072, 2011.

Ehret, G., Bousquet, P., Pierangelo, C., Alpers, M., Millet, B., Abshire, J. B., Bovensmann, H., Burrows, J. P., Chevallier, F., Ciais, P., et al.: MERLIN: A French-German space lidar mission dedicated to atmospheric methane, Remote Sensing, 9, 1052, 2017.

Emanuel, K. A.: A scheme for representing cumulus convection in large-scale models, Journal of the atmospheric sciences, 48, 2313–2329, 1991.

Etheridge, D., Pearman, G., and de Silva, F.: Atmospheric Trace-Gas Variations as Revealed by Air Trapped in an Ice Core from Law Dome, Antarctica, Annals of Glaciology, 10, 28–33, https://doi.org/10.3189/S0260305500004110, 1988.

European Space Agency (ESA): Launch of the first MetOp-SG satellite and Sentinel-5A, https://www.esa.int/Newsroom/Press_Releases/Lanzamiento_del_primer_satelite_MetOp-SG_y_del_Sentinel-5A, retrieved on November 19, 2025, 2025.

Forster, P., Storelvmo, T., Armour, K., Collins, W., Dufresne, J.-L., Frame, D., Lunt, D. J., Mauritsen, T., Palmer, M. D., Watanabe, M., Wild, M., and Zhang, H.: The Earth's Energy Budget, Climate Feedbacks, and Climate Sensitivity, pp. 923–1054, Cambridge University Press, Cambridge, United Kingdom and New York, NY, USA, https://doi.org/10.1017/9781009157896.009, 2021.

Francey, R. J., Steele, L. P., and Langenfelds, R. L.: Global atmospheric sampling laboratory (GASLAB): Supporting and extending the Cape Grim trace gas programs, 1996.

Global Environmental Database (GED): Global Environmental Database, https://db.cger.nies.go.jp/ged/en/links/index.html?id=link1, 2024.

Gottwald, M., Krieg, E., Lichtenberg, G., Slijkhuis, S., Noël, S., Bramstedt, K., Bovensmann, H., von Savigny, C., Snel, R., and Krijger, M.: Nine years of atmospheric remote sensing with SCIAMACHY-instrument performance, in: 2011 IEEE International Geoscience and Remote Sensing Symposium, pp. 3538–3541, IEEE, 2011.

Grandpeix, J.-Y. and Lafore, J.-P.: A density current parameterization coupled with Emanuel's convection scheme. Part I: The models, Journal of the Atmospheric Sciences, 67, 881–897, 2010.

https://doi.org/10.5194/egusphere-2025-5923
Preprint. Discussion started: 23 December 2025

Grandpeix, J.-Y., Lafore, J.-P., and Cheruy, F.: A density current parameterization coupled with Emanuel's convection scheme. Part II: 1D simulations, Journal of the Atmospheric Sciences, 67, 898–922, 2010.

Hauglustaine, D., Hourdin, F., Jourdain, L., Filiberti, M.-A., Walters, S., Lamarque, J.-F., and Holland, E. A.: Interactive chemistry in the Laboratoire de Météorologie Dynamique general circulation model: Description and background tropospheric chemistry evaluation, Journal of Geophysical Research: Atmospheres, 109, 2004.

Hourdin, F., Jam, A., Rio, C., Couvreux, F., Sandu, I., Lefebvre, M.-P., Brient, F., and Idelkadi, A.: Unified parameterization of convective boundary layer transport and clouds with the thermal plume model, Journal of Advances in Modeling Earth Systems, 11, 2910–2933, 2019.

Hourdin, F., Rio, C., Grandpeix, J.-Y., Madeleine, J.-B., Cheruy, F., Rochetin, N., Jam, A., Musat, I., Idelkadi, A., Fairhead, L., et al.: LMDZ6A: The atmospheric component of the IPSL climate model with improved and better tuned physics, Journal of Advances in Modeling Earth Systems, 12, e2019MS001 892, 2020.

Houweling, S., Bergamaschi, P., Chevallier, F., Heimann, M., Kaminski, T., Krol, M., Michalak, A. M., and Patra, P.: Global inverse modeling of CH 4 sources and sinks: an overview of methods, Atmospheric chemistry and physics, 17, 235–256, 2017.

Hu, H., Hasekamp, O., Butz, A., Galli, A., Landgraf, J., Aan de Brugh, J., Borsdorff, T., Scheepmaker, R., and Aben, I.: The operational methane retrieval algorithm for TROPOMI, Atmospheric Measurement Techniques, 9, 5423–5440, 2016.

Hungershoefer, K., Breon, F.-M., Peylin, P., Chevallier, F., Rayner, P., Klonecki, A., Houweling, S., and Marshall, J.: Evaluation of various observing systems for the global monitoring of CO 2 surface fluxes, Atmospheric chemistry and physics, 10, 10 503–10 520, 2010.

ICOS Research Infrastructure: ICOS Near Real-Time (Level 1) Atmospheric Greenhouse Gas Mole Fractions of CO2, CO and CH4, growing time series starting from latest Level 2 release (Version 1.0), https://doi.org/10.18160/ATM_NRT_CO2_CH4, accessed on 2021-06, 2018.

Ito, A. and Inatomi, M.: Water-use efficiency of the terrestrial biosphere: a model analysis focusing on interactions between the global carbon and water cycles, Journal of Hydrometeorology, 13, 681–694, 2012.

Jacob, D., Turner, A., Maasakkers, J., Sheng, J., Sun, K., and Liu, X., e. a.: Satellite observations of atmospheric methane and their value for quantifying methane emissions, Atmospheric Chemistry and Physics, 16, 14 371–14 396, 2016.

Jacob, D. J., Varon, D. J., Cusworth, D. H., Dennison, P. E., Frankenberg, C., Gautam, R., Guanter, L., Kelley, J., McKeever, J., Ott, L. E., et al.: Quantifying methane emissions from the global scale down to point sources using satellite observations of atmospheric methane, Atmospheric Chemistry and Physics Discussions, 2022, 1–44, 2022.

Kaiser, J., Heil, A., Andreae, M., Benedetti, A., Chubarova, N., Jones, L., Morcrette, J.-J., Razinger, M., Schultz, M., Suttie, M., et al.: Biomass burning emissions estimated with a global fire assimilation system based on observed fire radiative power, Biogeosciences, 9, 527–554, 2012.

Kopacz, M., Jacob, D. J., Fisher, J., Logan, J. A., Zhang, L., Megretskaia, I. A., Yantosca, R. M., Singh, K., Henze, D. K., Burrows, J., et al.: Global estimates of CO sources with high resolution by adjoint inversion of multiple satellite datasets (MOPITT, AIRS, SCIAMACHY, TES), Atmospheric Chemistry and Physics, 10, 855–876, 2010.

Lan, X., Thoning, K., and Dlugokencky, E.: Trends in globally-averaged CH4, N2O, and SF6 determined from NOAA Global Monitoring Laboratory measurements, Version 2025-09, https://doi.org/10.15138/P8XG-AA10, 2022.

Liang, R., Zhang, Y., Chen, W., Zhang, P., Liu, J., Chen, C., Mao, H., Shen, G., Qu, Z., Chen, Z., et al.: East Asian methane emissions inferred from high-resolution inversions of GOSAT and TROPOMI observations: a comparative and evaluative analysis, Atmospheric Chemistry and Physics, 23, 8039–8057, 2023.

https://doi.org/10.5194/egusphere-2025-5923
Preprint. Discussion started: 23 December 2025

Liu, X., Mizzi, A. P., Anderson, J. L., Fung, I. Y., and Cohen, R. C.: Assimilation of satellite NO 2 observations at high spatial resolution using OSSEs, Atmospheric Chemistry and Physics, 17, 7067–7081, 2017.

Locatelli, R., Bousquet, P., Chevallier, F., Fortems-Cheney, A., Szopa, S., Saunois, M., Agusti-Panareda, A., Bergmann, D., Bian, H., Cameron-Smith, P., et al.: Impact of transport model errors on the global and regional methane emissions estimated by inverse modelling, Atmospheric Chemistry and Physics, 13, 9917–9937, 2013.

Locatelli, R., Bousquet, P., Saunois, M., Chevallier, F., and Cressot, C.: Sensitivity of the recent methane budget to LMDz sub-grid-scale physical parameterizations, Atmospheric Chemistry and Physics, 15, 9765–9780, 2015.

Lopez, M., Schmidt, M., Ramonet, M., Bonne, J. L., Colomb, A., Kazan, V., and et al: Three years of semicontinuous greenhouse gas measurements at the Puy de Dôme station (central France), Atmospheric Measurement Techniques, 8, 3941–3958, 2015.

Lorente, A., Borsdorff, T., Butz, A., Hasekamp, O., aan de Brugh, J., Schneider, A., Wu, L., Hase, F., Kivi, R., Wunch, D., et al.: Methane retrieved from TROPOMI: improvement of the data product and validation of the first 2 years of measurements, Atmospheric Measurement Techniques, 14, 665–684, 2021.

Lu, X., Jacob, D. J., Zhang, Y., Maasakkers, J. D., Sulprizio, M. P., Shen, L., Qu, Z., Scarpelli, T. R., Nesser, H., Yantosca, R. M., et al.: Global methane budget and trend, 2010–2017: complementarity of inverse analyses using in situ (GLOBALVIEWplus CH 4 ObsPack) and satellite (GOSAT) observations, Atmospheric Chemistry and Physics, 21, 4637–4657, 2021.

Lund Myhre, C., Platt, S. M., Hermansen, O., Lunder, C., and Ri, I.: ICOS Atmosphere Level 2 data, Zeppelin, release 2022-1, Collection of ICOS ATC ASCII files, https://doi.org/10.18160/DVRW-N591, 2022.

Maksyutov, S., Oda, T., Saito, M., Janardanan, R., Belikov, D., Kaiser, J. W., Zhuravlev, R., Ganshin, A., Valsala, V. K., Andrews, A., Chmura, L., Dlugokencky, E., Haszpra, L., Langenfelds, R. L., Machida, T., Nakazawa, T., Ramonet, M., Sweeney, C., and Worthy, D.: Technical note: A high-resolution inverse modelling technique for estimating surface CO_2 fluxes based on the NIES-TM–FLEXPART coupled transport model and its adjoint, Atmospheric Chemistry and Physics, 21, 1245–1266, https://doi.org/10.5194/acp-21-1245-2021, 2021.

Masarie, K. and Tans, P.: Extension and integration of atmospheric carbon dioxide data into a globally consistent measurement record, Journal of Geophysical Research: Atmospheres, 100, 11 593–11 610, https://doi.org/10.1029/95JD00859, 1995.

Masarie, K. A., Langenfelds, R. L., Allison, C. E., Conway, T. J., Dlugokencky, E. J., Francey, R. J., Novelli, P. C., Steele, L. P., Tans, P. P., Vaughn, B., and White, J. W. C.: NOAA/CSIRO Flask Air Intercomparison Experiment: A strategy for directly assessing consistency among atmospheric measurements made by independent laboratories, Journal of Geophysical Research: Atmospheres, 106, 20 445–20 464, https://doi.org/https://doi.org/10.1029/2000JD000023, 2001.

Masutani, M., Woollen, J. S., Lord, S. J., Emmitt, G. D., Kleespies, T. J., Wood, S. A., Greco, S., Sun, H., Terry, J., Kapoor, V., et al.: Observing system simulation experiments at the National Centers for Environmental Prediction, Journal of Geophysical Research: Atmospheres, 115, 2010.

Meirink, J. F., Bergamaschi, P., and Krol, M. C.: Four-dimensional variational data assimilation for inverse modelling of atmospheric methane emissions: method and comparison with synthesis inversion, Atmospheric chemistry and physics, 8, 6341–6353, 2008.

Monforti Ferrario, F., Crippa, M., Guizzardi, D., Muntean, M., Schaaf, E., Lo Vullo, E., Solazzo, E., Olivier, J., and Vignati, E.: EDGAR v6.0 Greenhouse Gas Emissions, https://doi.org/10.2904/JRC_DATASET_EDGAR, 2021.

Monteil, G., Houweling, S., Butz, A., Guerlet, S., Schepers, D., Hasekamp, O., Frankenberg, C., Scheepmaker, R., Aben, I., and Röckmann, T.: Comparison of CH4 inversions based on 15 months of GOSAT and SCIAMACHY observations, Journal of Geophysical Research: Atmospheres, 118, 11–807, 2013.

https://doi.org/10.5194/egusphere-2025-5923
Preprint. Discussion started: 23 December 2025

Myhre, G., Shindell, D., Bréon, F.-M., Collins, W., Fuglestvedt, J., Huang, J., Koch, D., Lamarque, J.-F., Lee, D., Mendoza, B., et al.: Anthropogenic and natural radiative forcing, pp. 659–740, Cambridge University Press, 2014.

NIES GOSAT Data Archive Service: GOSAT [data set], https://data2.gosat.nies.go.jp/index_en.html, 2023.

O'Connor, F. M., Abraham, N. L., Dalvi, M., Folberth, G. A., Griffiths, P. T., Hardacre, C., Johnson, B. T., Kahana, R., Keeble, J., Kim, B., Morgenstern, O., Mulcahy, J. P., Richardson, M., Robertson, E., Seo, J., Shim, S., Teixeira, J. C., Turnock, S. T., Williams, J., Wiltshire, A. J., Woodward, S., and Zeng, G.: Assessment of pre-industrial to present-day anthropogenic climate forcing in UKESM1, Atmospheric Chemistry and Physics, 21, 1211–1243, https://doi.org/10.5194/acp-21-1211-2021, 2021.

Palmer, P. I., Feng, L., Lunt, M. F., Parker, R. J., Bösch, H., Lan, X., Lorente, A., and Borsdorff, T.: The added value of satellite observations of methane for understanding the contemporary methane budget, Philosophical Transactions of the Royal Society A, 379, 20210 106, 2021.

Parker, R. and Boesch, H.: University of Leicester GOSAT Proxy XCH4 v9.0, https://doi.org/10.5285/18ef8247f52a4cb6a14013f8235cc1eb, 2020.

Parker, R., Webb, A., Boesch, H., Somkuti, P., G., B., and Di Noia, A., e. a.: A decade of GOSAT Proxy satellite CH_4 observations, Earth System Science Data, 12, 3383–3412, https://doi.org/10.5194/essd-12-3383-2020, 2020.

Peters, W., Miller, J., Whitaker, J., Denning, A., Hirsch, A., Krol, M., Zupanski, D., Bruhwiler, L., and Tans, P.: An ensemble data assimilation system to estimate CO2 surface fluxes from atmospheric trace gas observations, Journal of Geophysical Research: Atmospheres, 110, 2005.

Pison, I.: Assimilation of atmospheric data for the optimization of trace gas emissions: from air quality to climate, Tech. rep., Universite de Versailles-Saint-Quentin-en-Yvelines, 2018.

Pison, I., Bousquet, P., Chevallier, F., Szopa, S., and Hauglustaine, D.: Multi-species inversion of CH4, CO and H2 emissions from surface measurements, Atmospheric Chemistry and Physics, 9, 5281–5297, 2009.

Potier, E., Broquet, G., Wang, Y., Santaren, D., Berchet, A., Pison, I., Marshall, J., Ciais, P., Bréon, F.-M., and Chevallier, F.: Complementing XCO 2 imagery with ground-based CO 2 and 14 CO 2 measurements to monitor CO 2 emissions from fossil fuels on a regional to local scale, Atmospheric Measurement Techniques, 15, 5261–5288, 2022.

Prinn, R. G., Weiss, R. F., Arduini, J., Arnold, T., DeWitt, H. L., Fraser, P. J., Ganesan, A. L., Gasore, J., Harth, C. M., Hermansen, O., et al.: History of chemically and radiatively important atmospheric gases from the Advanced Global Atmospheric Gases Experiment (AGAGE), Earth System Science Data Discussions, 2018, 1–39, 2018.

Qu, Z., Jacob, D. J., Shen, L., Lu, X., Zhang, Y., Scarpelli, T. R., Nesser, H., Sulprizio, M. P., Maasakkers, J. D., Bloom, A. A., et al.: Global distribution of methane emissions: a comparative inverse analysis of observations from the TROPOMI and GOSAT satellite instruments, Atmospheric Chemistry and Physics, 21, 14 159–14 175, 2021.

Reuter, M., Hilker, M., Noël, S., Di Noia, A., Weimer, M., Schneising, O., Buchwitz, M., Bovensmann, H., Burrows, J. P., Bösch, H., et al.: Retrieving the atmospheric concentrations of carbon dioxide and methane from the European Copernicus CO2M satellite mission using artificial neural networks, Atmospheric Measurement Techniques, 18, 241–264, 2025.

Ritter, F.: A procedure to clean, decompose, and aggregate time series, Hydrology and Earth System Sciences, 27, 349–361, 2023.

Saunois, M., Bousquet, P., Poulter, B., Peregon, A., Ciais, P., Canadell, J. G., Dlugokencky, E. J., Etiope, G., Bastviken, D., Houweling, S., et al.: The global methane budget: 2000–2012, Earth System Science Data Discussions, 2016, 1–79, 2016.

Saunois, M., Martinez, A., Poulter, B., Zhang, Z., Raymond, P. A., Regnier, P., Canadell, J. G., Jackson, R. B., Patra, P. K., Bousquet, P., Ciais, P., Dlugokencky, E. J., Lan, X., Allen, G. H., Bastviken, D., Beerling, D. J., Belikov, D. A., Blake, D. R., Castaldi, S., Crippa,

https://doi.org/10.5194/egusphere-2025-5923
Preprint. Discussion started: 23 December 2025

M., Deemer, B. R., Dennison, F., Etiope, G., Gedney, N., Höglund-Isaksson, L., Holgerson, M. A., Hopcroft, P. O., Hugelius, G., Ito, A., Jain, A. K., Janardanan, R., Johnson, M. S., Kleinen, T., Krummel, P. B., Lauerwald, R., Li, T., Liu, X., McDonald, K. C., Melton, J. R., Mühle, J., Müller, J., Murguia-Flores, F., Niwa, Y., Noce, S., Pan, S., Parker, R. J., Peng, C., Ramonet, M., Riley, W. J., Rocher-Ros, G., Rosentreter, J. A., Sasakawa, M., Segers, A., Smith, S. J., Stanley, E. H., Thanwerdas, J., Tian, H., Tsuruta, A., Tubiello, F. N., Weber, T. S., van der Werf, G. R., Worthy, D. E. J., Xi, Y., Yoshida, Y., Zhang, W., Zheng, B., Zhu, Q., Zhu, Q., and Zhuang, Q.: Global Methane Budget 2000–2020, Earth System Science Data, 17, 1873–1958, https://doi.org/10.5194/essd-17-1873-2025, 2025.

Schneider, M., Ertl, B., Tu, Q., Diekmann, C. J., Khosrawi, F., Röhling, A. N., Hase, F., Dubravica, D., García, O. E., Sepúlveda, E., Borsdorff, T., Landgraf, J., Lorente, A., Butz, A., Chen, H., Kivi, R., Laemmel, T., Ramonet, M., Crevoisier, C., Pernin, J., Steinbacher, M., Meinhardt, F., Strong, K., Wunch, D., Warneke, T., Roehl, C., Wennberg, P. O., Morino, I., Iraci, L. T., Shiomi, K., Deutscher, N. M., Griffith, D. W. T., Velazco, V. A., and Pollard, D. F.: Synergetic use of IASI profile and TROPOMI total-column level 2 methane retrieval products, Atmospheric Measurement Techniques, 15, 4339–4371, https://doi.org/10.5194/amt-15-4339-2022, 2022.

Schneising, O.: Product User Guide (PUG) TROPOMI WFM-DOAS (TROPOMI/WFMD) XCH4, 2021.

Schneising, O., Buchwitz, M., Reuter, M., Bovensmann, H., Burrows, J. P., Borsdorff, T., Deutscher, N. M., Feist, D. G., Griffith, D. W. T., Hase, F., Hermans, C., Iraci, L. T., Kivi, R., Landgraf, J., Morino, I., Notholt, J., Petri, C., Pollard, D. F., Roche, S., Shiomi, K., Strong, K., Sussmann, R., Velazco, V. A., Warneke, T., and Wunch, D.: A scientific algorithm to simultaneously retrieve carbon monoxide and methane from TROPOMI onboard Sentinel-5 Precursor, Atmospheric Measurement Techniques, 12, 6771–6802, https://doi.org/10.5194/amt-12-6771-2019, 2019.

Schneising, O., Buchwitz, M., Hachmeister, J., Vanselow, S., Reuter, M., Buschmann, M., Bovensmann, H., and Burrows, J. P.: Advances in retrieving XCH 4 and XCO from Sentinel-5 Precursor: improvements in the scientific TROPOMI/WFMD algorithm, Atmospheric Measurement Techniques, 16, 669–694, 2023.

Schuldt, K. N., Aalto, T., Andrews, A., Aoki, S., Arduini, J., Baier, B., Bergamaschi, P., Biermann, T., Biraud, S. C., Boenisch, H., Brailsford, G., Chen, H., Colomb, A., Conil, S., Cristofanelli, P., Cuevas, E., Daube, B., Davis, K., Mazière, M. D., Delmotte, M., Desai, A., DiGangi, J. P., Dlugokencky, E., Elkins, J. W., Emmenegger, L., Fischer, M. L., Gatti, L. V., Gehrlein, T., Gerbig, C., Gloor, E., Goto, D., Haszpra, L., Hatakka, J., Heimann, M., Heliasz, M., Hermanssen, O., Hintsa, E., Holst, J., Ivakhov, V., Jaffe, D., Joubert, W., Kang, H.-Y., Karion, A., Kazan, V., Keronen, P., Ko, M.-Y., Kominkova, K., Kort, E., Kozlova, E., Krummel, P., Kubistin, D., Labuschagne, C., Langenfelds, R., Laurent, O., Laurila, T., Lauvaux, T., Lee, J., Lee, H., Lee, C.-H., Lehner, I., Leppert, R., Leuenberger, M., Lindauer, M., Loh, Z., Lopez, M., Machida, T., Mammarella, I., Manca, G., Marek, M. V., Martin, M. Y., Matsueda, H., McKain, K., Miles, N., Miller, C. E., Miller, J. B., Moore, F., Morimoto, S., Munro, D., Myhre, C. L., Mölder, M., Müller-Williams, J., Nichol, S., Niwa, Y., O'Doherty, S., Obersteiner, F., Piacentino, S., Pichon, J. M., Pittman, J., Plass-Duelmer, C., Ramonet, M., Richardson, S., Rivas, P. P., Saito, K., Santoni, G., Sasakawa, M., Scheeren, B., Schuck, T., Schumacher, M., Seifert, T., Sha, M. K., Shepson, P., Sloop, C. D., Smith, P., Steinbacher, M., Stephens, B., Sweeney, C., Timas, H., Torn, M., Trisolino, P., Turnbull, J., Tørseth, K., Viner, B., Vitkova, G., Watson, A., Wofsy, S., Worsey, J., Worthy, D., Zahn, A., and di Sarra, A. G.: Multi-laboratory compilation of atmospheric methane data for the period 1983-2020, obspack_ch4_1_GLOBALVIEWplus_v4.0_2021-10-14; NOAA Earth System Research Laboratory, Global Monitoring Laboratory, https://doi.org/10.25925/20211001, 2021a.

Schuldt, K. N., Jacobson, A. R., Aalto, T., Andrews, A., Bergamaschi, P., Biermann, T., Biraud, S. C., Chen, H., Colomb, A., Conil, S., Cristofanelli, P., Mazière, M. D., Delmotte, M., Desai, A., Dlugokencky, E., Emmenegger, L., Fischer, M. L., Hatakka, J., Heliasz, M., Hermanssen, O., Holst, J., Jaffe, D., Karion, A., Kazan, V., Keronen, P., Kominkova, K., Kubistin, D., Laurent, O., Laurila, T., Lee, J., Lehner, I., Leuenberger, M., Lindauer, M., Lopez, M., Mammarella, I., Manca, G., Marek, M. V., McKain, K., Miller, J. B., Miller, C. E.,

https://doi.org/10.5194/egusphere-2025-5923
Preprint. Discussion started: 23 December 2025

Myhre, C. L., Mölder, M., Müller-Williams, J., Piacentino, S., Pichon, J. M., Plass-Duelmer, C., Ramonet, M., Scheeren, B., Schumacher, M., Sha, M. K., Sloop, C. D., Smith, P., Steinbacher, M., Sweeney, C., Trisolino, P., Tørseth, K., Viner, B., Vitkova, G., and di Sarra, A. G.: Multi-laboratory compilation of atmospheric methane data for the period 2006-2021, obspack_ch4_1_NRT_v3.0_2021-05-18; NOAA Earth System Research Laboratory, Global Monitoring Laboratory, https://doi.org/10.25925/20210518, 2021b.

Sicsik-Paré, A., Fortems-Cheiney, A., Pison, I., Broquet, G., Opler, A., Potier, E., Martinez, A., Schneising, O., Buchwitz, M., Maasakkers, J. D., et al.: Can we obtain consistent estimates of the emissions in Europe from three different CH4 TROPOMI products?, EGUsphere, 2025, 1–48, 2025.

Siddans, R., Knappett, D., Kerridge, B., Waterfall, A., Hurley, J., Latter, B., Boesch, H., and Parker, R.: Global height-resolved methane retrievals from the Infrared Atmospheric Sounding Interferometer (IASI) on MetOp, Atmospheric Measurement Techniques, 10, 4135–4164, 2017.

Simpson, I. J., Sulbaek Andersen, M. P., Meinardi, S., Bruhwiler, L., Blake, N. J., Helmig, D., Rowland, F. S., and Blake, D. R.: Long-term decline of global atmospheric ethane concentrations and implications for methane, Nature, 488, 490–494, 2012.

Someya, Y., Yoshida, Y., Ohyama, H., Nomura, S., Kamei, A., Morino, I., and et al.: Update on the GOSAT TANSO–FTS SWIR Level 2 retrieval algorithm, Atmospheric Measurement Techniques, 16, 1477–1501, https://doi.org/10.5194/amt-16-1477-2023, 2023.

Stull, R.: An introduction to boundary layer meteorology, vol. 13, Springer Science & Business Media, 1988.

Szopa, S., Naik, V., Adhikary, B., Artaxo, P., Berntsen, T., Collins, W., Fuzzi, S., Gallardo, L., Kiendler-Scharr, A., Klimont, Z., et al.: Short-lived climate forcers Climate Change 2021: The Physical Science Basis. Contribution of Working Group I to the Sixth Assessment Report of the Intergovernmental Panel on Climate Change, Climate Change 2021: The Physical Science Basis. Contribution of Working Group I to the Sixth Assessment Report of the Intergovernmental Panel on Climate Change, pp. 817–922, 2021a.

Szopa, S., Naik, V., Adhikary, B., Artaxo, P., Berntsen, T., Collins, W. D., Fuzzi, S., Gallardo, L., Kiendler-Scharr, A., Klimont, Z., Liao, H., Unger, N., and Zanis, P.: Short-Lived Climate Forcers, pp. 817–922, Cambridge University Press, Cambridge, United Kingdom and New York, NY, USA, https://doi.org/10.1017/9781009157896.008, 2021b.

Tanimoto, H., Matsunaga, T., Someya, Y., Fujinawa, T., Ohyama, H., Morino, I., Yashiro, H., Sugita, T., Inomata, S., Müller, A., et al.: The greenhouse gas observation mission with Global Observing SATellite for Greenhouse gases and Water cycle (GOSAT-GW): objectives, conceptual framework and scientific contributions, Progress in Earth and Planetary Science, 12, 1–33, 2025.

Thanwerdas, J., Saunois, M., Pison, I., Hauglustaine, D., Berchet, A., Baier, B., Sweeney, C., and Bousquet, P.: How do Cl concentrations matter for simulating CH 4, δ 13 C (CH 4) and estimating CH 4 budget through atmospheric inversions?, Atmospheric Chemistry and Physics Discussions, 2021, 1–23, 2021.

Thanwerdas, J., Saunois, M., Berchet, A., Pison, I., Vaughn, B., Michel, S., and Bousquet, P.: Variational Inverse Modelling within the Community Inversion Framework to Assimilate δ13C (CH_4) and CH_4: A Case Study with Model LMDz-SACS, Geoscientific Model Development Discussions, 2021, 1–29, 2022.

Thanwerdas, J., Saunois, M., Berchet, A., Pison, I., and Bousquet, P.: Investigation of the renewed methane growth post-2007 with high-resolution 3-D variational inverse modeling and isotopic constraints, Atmospheric Chemistry and Physics, 24, 2129–2167, 2024.

Thompson, R. L., Sasakawa, M., Machida, T., Aalto, T., Worthy, D., Lavric, J. V., Lund Myhre, C., and Stohl, A.: Methane fluxes in the high northern latitudes for 2005–2013 estimated using a Bayesian atmospheric inversion, Atmospheric Chemistry and Physics, 17, 3553–3572, 2017.

https://doi.org/10.5194/egusphere-2025-5923
Preprint. Discussion started: 23 December 2025

Tsuruta, A., Aalto, T., Backman, L., Hakkarainen, J., Van Der Laan-Luijkx, I. T., Krol, M. C., Spahni, R., Houweling, S., Laine, M., Dlugokencky, E., et al.: Global methane emission estimates for 2000–2012 from CarbonTracker Europe-CH 4 v1. 0, Geoscientific model development, 10, 1261–1289, 2017.

Tsuruta, A., Kuze, A., Shiomi, K., Kataoka, F., Kikuchi, N., Aalto, T., Backman, L., Kivimäki, E., Tenkanen, M. K., McKain, K., et al.: Global CH 4 Fluxes Derived from JAXA/GOSAT Lower Tropospheric Partial Column Data and the CTE-CH 4 Atmospheric Inverse Model, EGUsphere, 2025, 1–46, 2025.

UNFCCC: Report of the Conference of the Parties on its Nineteenth Session, held in Warsaw from 11 to 23 November 2013, in: United Nations Framework Convention on Climate Change, 2014.

Veefkind, J., Aben, I., McMullan, K., Förster, H., de Vries, J., Otter, G., Claas, J., Eskes, H., de Haan, J., Kleipool, Q., van Weele, M., Hasekamp, O., Hoogeveen, R., Landgraf, J., Snel, R., Tol, P., Ingmann, P., Voors, R., Kruizinga, B., Vink, R., Visser, H., and Levelt, P.: TROPOMI on the ESA Sentinel-5 Precursor: A GMES mission for global observations of the atmospheric composition for climate, air quality and ozone layer applications, Remote Sensing of Environment, 120, 70–83, https://doi.org/https://doi.org/10.1016/j.rse.2011.09.027, the Sentinel Missions - New Opportunities for Science, 2012.

Wang, F., Maksyutov, S., Tsuruta, A., Janardanan, R., Ito, A., Sasakawa, M., Machida, T., Morino, I., Yoshida, Y., Kaiser, J. W., et al.: Methane emission estimates by the global high-resolution inverse model using national inventories, Remote Sensing, 11, 2489, 2019.

Wang, Z., Warneke, T., Deutscher, N. M., Notholt, J., Karstens, U., Saunois, M., Schneider, M., Sussmann, R., Sembhi, H., Griffith, D. W., et al.: Contributions of the troposphere and stratosphere to CH 4 model biases, Atmospheric Chemistry and Physics, 17, 13 283–13 295, 2017.

Weber, T., Wiseman, N. A., and Kock, A.: Global ocean methane emissions dominated by shallow coastal waters, Nature communications, 10, 4584, 2019.

WMO-GAW Programme: CSIRO Greenhouse Gas Observations, https://gaw.kishou.go.jp, 2023.

Worden, J., Wecht, K., Frankenberg, C., Alvarado, M., Bowman, K., Kort, E., Kulawik, S., Lee, M., Payne, V., and Worden, H.: CH 4 and CO distributions over tropical fires during October 2006 as observed by the Aura TES satellite instrument and modeled by GEOS-Chem, Atmospheric Chemistry and Physics, 13, 3679–3692, 2013.

Worden, J. R., Cusworth, D. H., Qu, Z., Yin, Y., Zhang, Y., Bloom, A. A., Ma, S., Byrne, B. K., Scarpelli, T., Maasakkers, J. D., et al.: The 2019 methane budget and uncertainties at 1° resolution and each country through Bayesian integration Of GOSAT total column methane data and a priori inventory estimates, Atmospheric Chemistry and Physics, 22, 6811–6841, 2022.

Yokota, T., Yoshida, Y., Eguchi, N., Ota, Y., Tanaka, T., Watanabe, H., and Maksyutov, S.: Global concentrations of CO_2 and CH_4 retrieved from GOSAT: First preliminary results, Sola, 5, 160–163, 2009.

Yoshida, Y., Kikuchi, N., Morino, I., Uchino, O., Oshchepkov, S., Bril, A., and et al.: Improvement of the retrieval algorithm for GOSAT SWIR XCO 2 and XCH4 and their validation using TCCON data, Atmospheric Measurement Techniques, 6, 1533–1547, 2013.

Yoshida, Y., Someya, Y., Ohyama, H., Morino, I., Matsunaga, T., Deutscher, N. M., Griffith, D. W., Hase, F., Iraci, L. T., Kivi, R., et al.: Quality evaluation of the column-averaged dry air mole fractions of carbon dioxide and methane observed by GOSAT and GOSAT-2, SOLA, 19, 173–184, 2023.

Zhang, Y., Jacob, D. J., Maasakkers, J. D., Sulprizio, M. P., Sheng, J. X., Gautam, R., and Worden, J.: Monitoring global tropospheric OH concentrations using satellite observations of atmospheric methane, Atmospheric Chemistry and Physics, 18, 15 959–15 973, 2018.

https://doi.org/10.5194/egusphere-2025-5923
Preprint. Discussion started: 23 December 2025

Zhao, Y., Saunois, M., Bousquet, P., Lin, X., Berchet, A., Hegglin, M. I., Canadell, J. G., Jackson, R. B., Dlugokencky, E. J., Langenfelds, R. L., et al.: Influences of hydroxyl radicals (OH) on top-down estimates of the global and regional methane budgets, Atmospheric Chemistry and Physics Discussions, 2020, 1–45, 2020.

Zheng, B., Chevallier, F., Ciais, P., Yin, Y., and Wang, Y.: On the role of the flaming to smoldering transition in the seasonal cycle of African fire emissions, Geophysical Research Letters, 45, 11–998, 2018.